Fourth-order gas-kinetic scheme for turbulence simulation with multi-dimensional WENO reconstruction

Liang Pan [a,*], Guiyu Cao [b], Kun Xu [c,d]

[a] *Laboratory of Mathematics and Complex Systems, School of Mathematical Science, Beijing Normal University, Beijing, China*
[b] *Department of Mechanics and Aerospace Engineering, Southern University of Science and Technology, Shenzhen, China*
[c] *Department of Mathematics, Hong Kong University of Science and Technology, Clear Water Bay, Kowloon, Hong Kong*
[d] *Shenzhen Research Institute, Hong Kong University of Science and Technology, Shenzhen, China*

ARTICLE INFO

ABSTRACT

In this paper, a fourth-order multi-dimensional weighted essentially non-oscillatory (WENO) reconstruction is developed, which is aiming at the complicated flows. In corporate with two-stage fourth-order temporal discretization, a high-order gas-kinetic scheme is proposed for the direct numerical simulation (DNS) and large eddy simulation (LES) of turbulence. In such WENO scheme, a simple strategy of selecting stencils is adopted and the topology independent linear weights are used. The fourth-order reconstruction improves the order of accuracy of the previous third-order WENO reconstruction [Computers and Fluids 198 (2020) 104401], which is too dissipative for the simulation of turbulent flows. Compared with the classical dimension-by-dimension WENO reconstruction, the order of accuracy can be also achieved for any non-uniform and curvilinear meshes in the finite volume framework. Numerical examples, including the classical turbulence cases, are provided to illustrate the good performance of such WENO scheme for turbulence simulation. More importantly, the fourth-order WENO scheme is robust and works well from the subsonic to hypersonic flows. In the future, the current scheme will be extended to the genuinely unstructured meshes for more complicated turbulent flows.

1. Introduction

Turbulence is an important research subject among physics, applied mathematics, and engineering applications [35]. Currently, there are mainly three approaches for turbulence simulation, namely direct numerical simulations (DNS), large eddy simulations (LES) and Reynolds averaged Navier–Stokes methods (RANS). DNS methods [25,31] resolve the turbulent structures above the Kolmogorov dissipation scale, which has been widely used for studying the turbulent mechanism with low-Reynolds number. LES methods [16,36,42] solve the filtered Navier–Stokes equations with resolvable turbulent structures above the inertial scale, gradually becoming an indispensable tool to obtain high-resolution unsteady turbulent flow fields. RANS methods [38,45] are the work-hoarse for engineering turbulence simulations, which capture turbulent structures above the integral scale under the constraints of computational resources.

To resolve small-scale flow structures and capture discontinuities in the compressible turbulent flow fields, the development of high-order schemes is a long-standing goal of computational fluid dynamics research. Until now, there have been a gigantic number of publications about the introduction and survey of high-order schemes, such as total variation diminishing (TVD) schemes [17], essentially non-oscillatory (ENO) schemes, weighted ENO (WENO) schemes and discontinuous Galerkin (DG) schemes [11,12], etc. The ENO schemes were proposed in Harten et al. [18], Shu and Osher [39] and successfully applied to solve the hyperbolic conservation laws and other convection dominated problems. Following the ENO schemes, the WENO schemes [23,28] were developed with the nonlinear convex combination of candidate polynomials. The WENO schemes achieve higher order of accuracy and keep non-oscillatory property essentially. However, the classical WENO schemes fail to recover the formal fifth-order accuracy near critical points, where the low-order derivatives vanish. To deal with this problem, WENO-M and WENO-Z methods [5,19] were developed. On the unstructured meshes, the WENO schemes were also developed [20,48], in which the high-order of accuracy is also obtained by the non-linear combination of lower order polynomials. However, its successful application is limited by the appearance of

* Corresponding author
E-mail addresses: panliang@bnu.edu.cn (L. Pan), gcaoaa@connect.ust.hk (G. Cao), makxu@ust.hk (K. Xu).

negative linear weights and very large linear weights. Instead of concentrating on the reconstruction of interface values, there exist another two classes of WENO methods to reconstruct a polynomial inside each cell based on all stencils, which is named as the WENO with adaptive order schemes [1,2,15] and simple WENO schemes [49–51]. The linear weights are topology independent and artificially set to be positive numbers, and the non-linear weights are chosen to achieve the optimal order of accuracy in the smooth region and suppress the oscillations near the discontinuous region. These WENO schemes not only improve the efficiency, but also reduce the complexity of the classical WENO scheme [20,48], especially for the unstructured meshes. However, they are rarely applied for the simulation of turbulent flows.

In the past decades, the gas-kinetic schemes (GKS) based on the Bhatnagar–Gross–Krook equation (BGK) [3,10] have been developed systematically for the computations from the low speed flows to supersonic ones [46,47]. Different from the numerical methods based on the Riemann solvers [41], a time-dependent numerical flux function is provided at a cell interface for inviscid and viscous terms together. Based on the time-dependent flux function, a two-stage fourth-order method was developed for the generalized Riemann problem solver [14,27] and gas-kinetic scheme [33]. In the construction of high-order schemes, a spatial-temporal coupled evolution model becomes important, and the delicate flow structures depend on the quality of flow solvers. With the high-order spatial reconstruction, a reliable framework was provided for the fourth-order and even higher-order schemes [21]. More importantly, the high-order gas-kinetic scheme is as robust as the second-order scheme and works perfectly from the subsonic flows to hypersonic ones. The gas-kinetic schemes have also been applied for the simulations of turbulent flows successfully. For high Reynolds number turbulent flows, the gas-kinetic scheme coupled with the traditional eddy viscosity turbulence model has been developed and implemented in the turbulence study [7,40]. The high-order gas-kinetic scheme has been also developed for the direct numerical simulation of isotropic compressible turbulence [8], which was the first attempt by gas-kinetic scheme to the DNS study.

Recently, more classical turbulent tests from nearly incompressible flows to the hypersonic ones are used to validate the parallel scalability, efficiency, accuracy, and robustness of HGKS, which verifies the validity for compressible turbulence study [9]. The dimension-by-dimension WENO reconstruction is used for spatial accuracy, and the meshes are considered to be locally uniform without special treatment. However, such reconstruction encounters difficulties for the flows with complicated geometry. One efficient way is to construct the high-order scheme in curvilinear coordinate system, and another way is to consider the mesh as an unstructured one. In the previous study [32], a third-order gas-kinetic scheme is developed on the three-dimensional structured meshes with the simple WENO type reconstruction, in which a simple strategy of selecting stencils for reconstruction is adopted and the topology independent linear weights are used. However, the third-order reconstruction is too dissipative for the simulation of turbulent flows, and the small scale is smeared severely. In this paper, a fourth-order WENO scheme is developed, which improves the order of accuracy with a larger stencil for reconstruction. The similar strategies are adopted for both selection stencils and non-linear weights. In corporate with the two-stage temporal discretization, a fourth-order gas-kinetic scheme is developed. Both accuracy and robustness are validated by the numerical examples. With the high-order spatial and temporal discretization, the gas-kinetic scheme can be used for the direct numerical simulation (DNS) and large eddy simulation (LES) of turbulence, and the classical turbulent tests are provided to illustrate the good performance of such WENO reconstruction. In the future, the current

scheme will be extended to the three-dimensional unstructured meshes for more complicated turbulent flows.

This paper is organized as follows. In Section 2, BGK equation and turbulent model are briefly reviewed. The fourth-order gas-kinetic scheme with the newly developed WENO reconstruction is given in Section 3. Section 4 includes numerical simulation and discussions. The last section is the conclusion.

2. BGK equation and turbulent model

The three-dimensional BGK equation [3,10] can be written as

$$f_t + uf_x + vf_y + wf_z = \frac{g - f}{\tau}, \tag{1}$$

where $\boldsymbol{u} = (u, v, w)$ is the particle velocity, f is the gas distribution function, g is the three-dimensional Maxwellian distribution and τ is the collision time. The collision term satisfies the compatibility condition

$$\int \frac{g - f}{\tau} \psi \, d\Xi = 0, \tag{2}$$

where $\psi = (1, u, v, w, \frac{1}{2}(u^2 + v^2 + w^2 + \varsigma^2))^T$, $\varsigma^2 = \varsigma_1^2 + \ldots + \varsigma_K^2$ is the internal variable, $d\Xi = du\,dv\,dw\,d\varsigma_1 \ldots d\varsigma_K$ and $K = (5 - 3\gamma)/(\gamma - 1)$ is the degree of freedom for the three-dimensional flows, where γ is the specific heat ratio. According to the Chapman–Enskog expansion for BGK equation, the macroscopic governing equations can be derived [46,47]. For the zeroth-order truncation $f = g$, the Euler equations can be obtained. For the first-order truncation

$$f = g - \tau(ug_x + vg_y + wg_z + g_t),$$

the Navier–Stokes equations can be obtained. With higher-order truncations, the Burnett and super-Burnett equations can be derived as well.

For the turbulence modeling, we follow the concept of turbulent eddy viscosity, which models the effect of unresolved turbulent scales by the enlarged turbulent eddy viscosity [7,40]. An extended BGK equation can be written as

$$f_t + uf_x + vf_y + wf_z = \frac{g - f}{\tau + \tau_t}, \tag{3}$$

where τ_t is an enlarged turbulent relaxation time proposed to describe the turbulent flows. Based on the Chapman–Enskog expansion, Eq. (3) can recover the eddy viscosity model according to the following relation between turbulent eddy viscosity μ_t and turbulent relaxation time τ_t

$$\tau + \tau_t = \frac{\mu + \mu_t}{p}, \tag{4}$$

where p is the pressure. In this paper, the large eddy simulation (LES) is considered. To keep the simple eddy viscosity closure form and overcome the drawbacks of the original Smagorinsky model, the Vreman-type model [42] is used and the turbulent eddy viscosity μ_t is given by

$$\mu_t = 2.5\rho C_s^2 \sqrt{\frac{B_\beta}{a_{ij}a_{ij}}}, \tag{5}$$

where ρ is the density and $C_s = 0.1$ is the Smagorinsky constant. The left unknowns above can be determined through the combination of velocity gradient in resolved flow fields

$$\begin{cases} \alpha_{ij} = \dfrac{\partial U_j}{\partial x_i}, \\ \beta_{ij} = \Delta_m^2 \alpha_{mi} \alpha_{mj}, \\ B_\beta = \beta_{11}\beta_{22} + \beta_{11}\beta_{33} + \beta_{22}\beta_{33} - \beta_{12}^2 - \beta_{13}^2 - \beta_{23}^2, \end{cases}$$

where Δ_m is the width of the numerical cell.

3. High-order gas-kinetic scheme

3.1. Finite volume scheme and gas-kinetic solver

In this paper, we mainly focus on the structured mesh. Taking moments of Eq. (1) and integrating with respect to space, the semi-discretized finite volume scheme for the hexahedron cell Ω_{ijk} can be obtained as follows

$$\frac{\partial Q_{ijk}}{\partial t} = \mathcal{L}(Q_{ijk}),$$

where Q_{ijk} is the cell averaged conservative value. The operator $\mathcal{L}$ is defined as

$$\mathcal{L}(Q_{ijk}) = -\frac{1}{|\Omega_{ijk}|} \sum_{p=1}^{6} \mathbb{F}_p(t) = -\frac{1}{|\Omega_{ijk}|} \sum_{p=1}^{6} \iint_{\Sigma_p} F(Q,t) \cdot \mathbf{n} d\sigma,$$

(6)

where $|\Omega_{ijk}|$ is the area of Ω_{ijk}, Σ_p is the cell interface of Ω_{ijk} and $\mathbf{n}$ is the outer normal direction. For some meshes, the vertexes of hexahedron cell maybe non-coplanar, and the high-order accuracy can not be achieved without evaluating the volume and integrals accurately. Thus, a trilinear interpolation is introduced for the hexahedron cell Ω_{ijk}

$$\mathbf{X}(\xi, \eta, \zeta) = \sum_{m=1}^{8} \mathbf{x}_m \psi_m(\xi, \eta, \zeta),$$

where $(\xi, \eta, \zeta) \in [-1/2, 1/2]^3$, $\mathbf{x}_m$ is the vertex of a hexahedron cell and the base function ψ_m is given as follows

$$\psi_1 = \frac{1}{8}(1 - 2\xi)(1 - 2\eta)(1 - 2\zeta),$$
$$\psi_2 = \frac{1}{8}(1 - 2\xi)(1 - 2\eta)(1 + 2\zeta),$$
$$\psi_3 = \frac{1}{8}(1 - 2\xi)(1 + 2\eta)(1 - 2\zeta),$$
$$\psi_4 = \frac{1}{8}(1 - 2\xi)(1 + 2\eta)(1 + 2\zeta),$$
$$\psi_5 = \frac{1}{8}(1 + 2\xi)(1 - 2\eta)(1 - 2\zeta),$$
$$\psi_6 = \frac{1}{8}(1 + 2\xi)(1 - 2\eta)(1 + 2\zeta),$$
$$\psi_7 = \frac{1}{8}(1 + 2\xi)(1 + 2\eta)(1 - 2\zeta),$$
$$\psi_8 = \frac{1}{8}(1 + 2\xi)(1 + 2\eta)(1 + 2\zeta).$$

In the computation, the Gaussian quadrature is used for the following triple integral over the hexahedron cell with non-coplanar vertexes

$$\iiint_{\Omega} x^a y^b z^c dx dy dz = \sum_{l,m,n=1}^{3} \omega_{lmn} x^a y^b z^c (\xi_l, \eta_m, \zeta_n)$$
$$\times \left| \frac{\partial(x,y,z)}{\partial(\xi,\eta,\zeta)} \right|_{(\xi_l,\eta_m,\zeta_n)} \Delta\xi \Delta\eta \Delta\zeta,$$

where ω_{lmn} is the Gaussian quadrature weight and (ξ_l, η_m, ζ_n) is the quadrature point. To achieve the spatial accuracy, the numerical integration is needed for the surface integral over the cell interface as well, and one of the numerical fluxes is given as an example

$$\mathbb{F}_p(t) = \iint_{\Sigma_p} F(Q) \cdot \mathbf{n} d\sigma = \int_{-1/2}^{1/2} \int_{-1/2}^{1/2} F(Q(\mathbf{X}(\eta,\zeta)))$$
$$\cdot \mathbf{n} \|\mathbf{X}_\eta \times \mathbf{X}_\zeta\| d\eta d\zeta$$

$$= \sum_{m_1,m_2=1}^{2} \omega_{m_1,m_2} F_{m_1,m_2}(t) \|\mathbf{X}_\eta$$
$$\times \mathbf{X}_\zeta\|_{m_1,m_2} \Delta\eta \Delta\zeta,$$

where ω_{m_1,m_2} is Gaussian quadrature weight. For the surface integral, the bilinear interpolation is used to parameterize the interface

$$\mathbf{X}(\eta, \zeta) = \sum_{m=1}^{4} \mathbf{x}_m \phi_m(\eta, \zeta),$$

where $(\eta, \zeta) \in [-1/2, 1/2]^2$, $\mathbf{x}_m$ is the vertex of the interface Σ_p and ϕ_m is the base function

$$\phi_1 = \frac{1}{4}(1 - 2\eta)(1 - 2\zeta), \quad \phi_2 = \frac{1}{4}(1 - 2\eta)(1 + 2\zeta),$$
$$\phi_3 = \frac{1}{4}(1 + 2\eta)(1 - 2\zeta), \quad \phi_4 = \frac{1}{4}(1 + 2\eta)(1 + 2\zeta).$$

With the bilinear interpolation above, a local coordinate can be given for each Gaussian quadrature point.

The numerical flux at Gaussian quadrature point in the global coordinate $F_{m_1,m_2}(t)$ can be obtained by taking moments of the gas distribution function

$$F_{m_1,m_2}(t) = \int \mathbf{u} \cdot \mathbf{n}_{m_1,m_2} \psi f(\mathbf{x}_{m_1,m_2}, t, \mathbf{u}, \varsigma) d\Xi.$$

(7)

In the actual computation, the reconstruction is performed in a local coordinate and a coordinate transformation is needed for the numerical fluxes. This procedure is similar with the numerical methods with Riemann solvers [41], and more details for gas-kinetic scheme can be found in Pan and Xu [32]. In the local coordinate, the gas distribution function is also denoted as $f(\mathbf{x}_{m_1,m_2}, t, \mathbf{u}, \varsigma)$ for simplicity. The integral solution of BGK equation Eq. (1) is used for the gas distribution function at cell interface

$$f(\mathbf{x}_{m_1,m_2}, t, \mathbf{u}, \varsigma) = \frac{1}{\tau} \int_0^t g(\mathbf{x}', t', \mathbf{u}, \varsigma) e^{-(t-t')/\tau} dt' + e^{-t/\tau} f_0(-\mathbf{u}t, \varsigma),$$

where $\mathbf{x}' = \mathbf{x}_{m_1,m_2} - \mathbf{u}(t - t')$ is the trajectory of particles, $\mathbf{u} = (u, v, w)$ is the particle velocity in the local coordinate, f_0 is the initial gas distribution function and g is the corresponding equilibrium state. With the reconstruction of macroscopic variables, the second-order gas distribution function at the cell interface can be expressed as

$$f(\mathbf{x}_{m_1,m_2}, t, \mathbf{u}, \varsigma) = (1 - e^{-t/\tau})g_0 + ((t + \tau)e^{-t/\tau} - \tau)(\bar{a}_1 u + \bar{a}_2 v + \bar{a}_3 w)g_0$$
$$+ (t - \tau + \tau e^{-t/\tau})\bar{A}g_0$$
$$+ e^{-t/\tau} g_r [1 - (\tau + t)(a_1^r u + a_2^r v + a_3^r w) - \tau A^r](1 - H(u))$$
$$+ e^{-t/\tau} g_l [1 - (\tau + t)(a_1^l u + a_2^l v + a_3^l w) - \tau A^l]H(u),$$

(8)

where g_l, g_r are the equilibrium states corresponding to the reconstructed variables Q_l, Q_r at both sides of cell interface, and the equilibrium state g_0 and corresponding conservative variable Q_0 are given by the compatibility condition Eq. (2)

$$\int \psi g_0 d\Xi = Q_0 = \int_{u>0} \psi g_l d\Xi + \int_{u<0} \psi g_r d\Xi.$$

The coefficients in Eq. (8) can be obtained by the reconstructed directional derivatives in the local coordinate ($\mathbf{n}_x, \mathbf{n}_y, \mathbf{n}_z$) and compatibility condition

$$\langle a_1^k \rangle = \frac{\partial Q_k}{\partial \mathbf{n}_x}, \langle a_2^k \rangle = \frac{\partial Q_k}{\partial \mathbf{n}_y}, \langle a_3^k \rangle = \frac{\partial Q_k}{\partial \mathbf{n}_z}, \langle a_1^k u + a_2^k v + a_3^k w + A^k \rangle = 0,$$

$$\langle \bar{a}_1 \rangle = \frac{\partial Q_0}{\partial \mathbf{n}_x}, \langle \bar{a}_2 \rangle = \frac{\partial Q_0}{\partial \mathbf{n}_y}, \langle \bar{a}_3 \rangle = \frac{\partial Q_0}{\partial \mathbf{n}_z}, \langle \bar{a}_1 u + \bar{a}_2 v + \bar{a}_3 w + \bar{A} \rangle = 0,$$

where $k = l, r$ and the moments of the equilibrium g and defined by

$$\langle \ldots \rangle = \int g(\ldots)\psi \mathrm{d}\Xi.$$

The construction of $\frac{\partial Q_{l,r}}{\partial \boldsymbol{n}_x}, \frac{\partial Q_{l,r}}{\partial \boldsymbol{n}_y}, \frac{\partial Q_{l,r}}{\partial \boldsymbol{n}_z}$ will be presented in the following section. In the classical gas-kinetic scheme, an extra reconstruction is needed for the equilibrium part. However, such reconstruction introduces extra difficulty for the genuinely multidimensional scheme [21]. In this section, the spatial derivatives for the equilibrium part can be determined as follows

$$\frac{\partial Q_0}{\partial \boldsymbol{n}_x} = \int_{u>0} \psi a_1^l g_l \mathrm{d}\Xi + \int_{u<0} \psi a_1^r g_r \mathrm{d}\Xi,$$

$$\frac{\partial Q_0}{\partial \boldsymbol{n}_y} = \int_{u>0} \psi a_2^l g_l \mathrm{d}\Xi + \int_{u<0} \psi a_2^r g_r \mathrm{d}\Xi,$$

$$\frac{\partial Q_0}{\partial \boldsymbol{n}_z} = \int_{u>0} \psi a_3^l g_l \mathrm{d}\Xi + \int_{u<0} \psi a_3^r g_r \mathrm{d}\Xi.$$

The procedure above reduces the complexity greatly. More details of the gas-kinetic scheme can be found in Xu [46].

3.2. Temporal discretization

The two-stage fourth-order method is used for temporal discretization, which was developed for Lax–Wendroff type solvers [14,27,33]. Consider the following time-dependent equation

$$\frac{\mathrm{d}Q}{\mathrm{d}t} = \mathcal{L}(Q),$$

where $\mathcal{L}$ is an operator for spatial derivative of flux given by Eq. (6), the state Q^{n+1} at $t_{n+1} = t_n + \Delta t$ can be updated with the following formula

$$Q^* = Q^n + \frac{1}{2}\Delta t \mathcal{L}(Q^n) + \frac{1}{8}\Delta t^2 \frac{\partial}{\partial t}\mathcal{L}(Q^n),$$

$$Q^{n+1} = Q^n + \Delta t \mathcal{L}(Q^n) + \frac{1}{6}\Delta t^2\left(\frac{\partial}{\partial t}\mathcal{L}(Q^n) + 2\frac{\partial}{\partial t}\mathcal{L}(Q^*)\right).$$

It can be proved that for hyperbolic equations the above temporal discretization provides a fourth-order time accurate solution [27]. To implement the two-stage method for Eq. (6), a linear function is used to approximate the time dependent numerical flux

$$\mathbb{F}_p(t) = \mathbb{F}_p^n + \partial_t \mathbb{F}_p^n(t - t_n). \tag{9}$$

Integrating Eq. (9) over $[t_n, t_n + \Delta t/2]$ and $[t_n, t_n + \Delta t]$, we have the following two equations

$$\mathbb{F}_p^n \Delta t + \frac{1}{2}\partial_t \mathbb{F}_p^n \Delta t^2 = \int_{t_n}^{t_n+\Delta t} \mathbb{F}_p(t)\mathrm{d}t,$$

$$\frac{1}{2}\mathbb{F}_p^n \Delta t + \frac{1}{8}\partial_t \mathbb{F}_p^n \Delta t^2 = \int_{t_n}^{t_n+\Delta t/2} \mathbb{F}_p(t)\mathrm{d}t.$$

The coefficients $\partial_t \mathbb{F}_p^n$ and $\partial_t \mathbb{F}_p^n$ can be determined by solving the linear system, and $\mathcal{L}(\Omega_{ijk}^n)$ and temporal derivative $\partial_t \mathcal{L}(\Omega_{ijk}^n)$ at t^n can be given by

$$\mathcal{L}(Q_{ijk}^n) = -\frac{1}{|\Omega_{ijk}|}\sum_{p=1}^{6}\mathbb{F}_p^n, \quad \partial_t\mathcal{L}(Q_{ijk}^n) = -\frac{1}{|\Omega_{ijk}|}\sum_{p=1}^{6}\partial_t\mathbb{F}_p^n.$$

Similarly, $\mathcal{L}(\Omega_{ijk}^*), \partial_t\mathcal{L}(\Omega_{ijk}^*)$ at the intermediate state can be constructed as well.

3.3. Spatial reconstruction

In our previous study, a third-order multi-dimensional WENO reconstruction was developed [32]. However, for the viscous flows
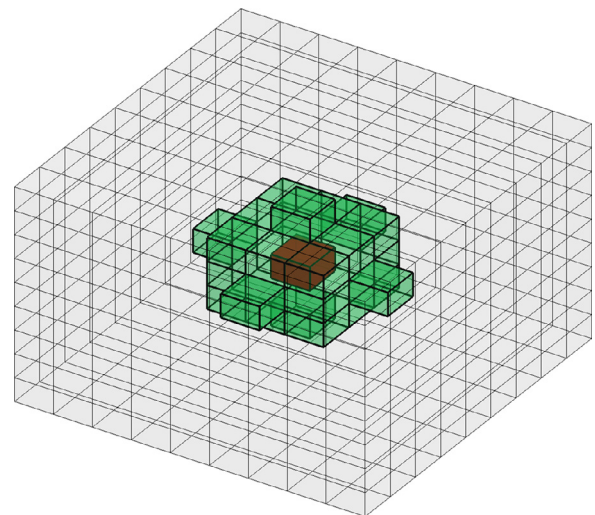

Fig. 1. Stencils for fourth-order reconstruction: the red cubic represents the cell Ω_{ijk} and the green cells represent the cells of big stencil. (For interpretation of the references to color in this figure legend, the reader is referred to the web version of this article.)

with moderate Reynolds numbers, the third-order scheme is too dissipative and a higher-order reconstruction is needed. In this section, a fourth-order WENO reconstruction is developed on the structured meshes and the extension to unstructured meshes will be developed in the future.

For a piecewise smooth function $q(\boldsymbol{x})$ over the cell Ω_{ijk}, a polynomial $P_0(\boldsymbol{x})$ with degree r can be constructed to approximate $q(\boldsymbol{x})$ as follows

$$P_0(\boldsymbol{x}) = q(\boldsymbol{x}) + \mathcal{O}(h^{r+1}),$$

where $h \sim |\Omega_{ijk}|^{1/3}$ is the cell size. In order to achieve the fourth-order accuracy and satisfy the conservative property, a cubic polynomial is constructed

$$P_0(\boldsymbol{x}) = Q_{ijk} + \sum_{|\boldsymbol{n}|=1}^{3} a_{\boldsymbol{n}} p_{\boldsymbol{n}}(\boldsymbol{x}), \tag{10}$$

where Q_{ijk} is the cell averaged variables of $Q(\boldsymbol{x})$ over Ω_{ijk}, $\boldsymbol{n} = (n_1, n_2, n_3)$ is the multi-index, $|\boldsymbol{n}| = n_1 + n_2 + n_3$ and

$$p_{\boldsymbol{n}}(\boldsymbol{x}) = x^{n_1}y^{n_2}z^{n_3} - \frac{1}{|\Omega_{ijk}|}\iiint_{\Omega_{ijk}} x^{n_1}y^{n_2}z^{n_3}\mathrm{d}V.$$

In order to fully determine this polynomial, a bigger stencil S shown in Fig. 1 for Ω_{ijk} is selected and the index of elements is rearranged as follows

$$S = \left\{\Omega_{i+i_0,j+j_0,k+k_0}, \ i_0, j_0, k_0 = -1, 0, 1\right\}\bigcup\left\{\Omega_{i\pm2,j,k}, \Omega_{i,j\pm2,k}, \Omega_{i,j,k\pm2}\right\}$$

$$= \left\{\Omega_n, n = 0, \ldots, 26\right\}\bigcup\left\{\Omega_n, n = 27, \ldots, 32\right\},$$

where $\Omega_0 = \Omega_{ijk}$. The following constrains need to be satisfied in the big stencil

$$\frac{1}{|\Omega_n|}\iiint_{\Omega_n} P_0(\boldsymbol{x})\mathrm{d}V = Q_n, \ \Omega_n \in S,$$

where Q_n is the conservative variable with newly rearranged index. To determine the cubic polynomial, an over-determined linear system is obtained

$$\mathbf{A} \cdot \mathbf{a} = \Delta\mathbf{Q},$$

where $\Delta\mathbf{Q} = (Q_1 - Q_0, \ldots, Q_{32} - Q_0)^T$, $\mathbf{a} = (a_1, \ldots, a_{19})^T$. The multi-index $\boldsymbol{n}$ is also rearranged and the coefficient matrix $\mathbf{A} = (A_{jk}), 1 \le j \le 32, 1 \le k \le 19$ is given as

$$A_{jk} = \frac{1}{|\Omega_j|}\iint_{\Omega_j} p_k(x, y)\mathrm{d}x\mathrm{d}y\mathrm{d}z.$$

For some cases, such as the turbulent channel flow, the reconstruction becomes unstable and a weighted least square method is used

$$(\mathbf{A}^T \mathbf{W} \mathbf{A}) \cdot \mathbf{a} = \mathbf{A}^T \mathbf{W} \triangle \mathbf{Q}, \tag{11}$$

where $\mathbf{W}$ is a diagonal matrix with $w_{ii} = 1, i = 1, \ldots, 26$ and $w_{ii} = 0.1, i = 27, \ldots, 32$.

To deal with the discontinuity, several linear polynomials are constructed based on the candidate sub-stencils

$$P_m(\boldsymbol{x}) = Q_{ijk} + \sum_{|\boldsymbol{n}|=1} b_{\boldsymbol{n}}^m p_{\boldsymbol{n}}(\boldsymbol{x}), \tag{12}$$

where $m = 1, \ldots M$ and M is the number of sub-stencils. In the previous paper [50], the sub-stencils $S'_m, m = 1, \ldots, 24$ are used and one third of them are given as follows

$$S'_1 = \{\Omega_{ijk}, \Omega_{i+1,j,k}, \Omega_{i,j+1,k}, \Omega_{i+1,j+1,k}, \Omega_{i,j,k+1}\},$$
$$S'_2 = \{\Omega_{ijk}, \Omega_{i-1,j,k}, \Omega_{i,j+1,k}, \Omega_{i-1,j+1,k}, \Omega_{i,j,k+1}\},$$
$$S'_3 = \{\Omega_{ijk}, \Omega_{i+1,j,k}, \Omega_{i,j-1,k}, \Omega_{i+1,j-1,k}, \Omega_{i,j,k+1}\},$$
$$S'_4 = \{\Omega_{ijk}, \Omega_{i-1,j,k}, \Omega_{i,j+1,k}, \Omega_{i-1,j-1,k}, \Omega_{i,j,k+1}\},$$
$$S'_5 = \{\Omega_{ijk}, \Omega_{i+1,j,k}, \Omega_{i,j+1,k}, \Omega_{i+1,j+1,k}, \Omega_{i,j,k-1}\},$$
$$S'_6 = \{\Omega_{ijk}, \Omega_{i-1,j,k}, \Omega_{i,j+1,k}, \Omega_{i-1,j+1,k}, \Omega_{i,j,k-1}\},$$
$$S'_7 = \{\Omega_{ijk}, \Omega_{i+1,j,k}, \Omega_{i,j-1,k}, \Omega_{i+1,j-1,k}, \Omega_{i,j,k-1}\},$$
$$S'_8 = \{\Omega_{ijk}, \Omega_{i-1,j,k}, \Omega_{i,j+1,k}, \Omega_{i-1,j-1,k}, \Omega_{i,j,k-1}\}.$$

However, such choice of sub-stencils costs more memory and reduces the efficiency of computation. A simplified version with eight sub-stencils is adopted for the fourth-order reconstruction

$$S_1 = \{\Omega_{ijk}, \Omega_{i+1,j,k}, \Omega_{i,j+1,k}, \Omega_{i,j,k+1}\},$$
$$S_5 = \{\Omega_{ijk}, \Omega_{i+1,j,k}, \Omega_{i,j+1,k}, \Omega_{i,j,k-1}\},$$
$$S_2 = \{\Omega_{ijk}, \Omega_{i-1,j,k}, \Omega_{i,j+1,k}, \Omega_{i,j,k+1}\},$$
$$S_6 = \{\Omega_{ijk}, \Omega_{i-1,j,k}, \Omega_{i,j+1,k}, \Omega_{i,j,k-1}\},$$
$$S_3 = \{\Omega_{ijk}, \Omega_{i+1,j,k}, \Omega_{i,j-1,k}, \Omega_{i,j,k+1}\},$$
$$S_7 = \{\Omega_{ijk}, \Omega_{i+1,j,k}, \Omega_{i,j-1,k}, \Omega_{i,j,k-1}\},$$
$$S_4 = \{\Omega_{ijk}, \Omega_{i-1,j,k}, \Omega_{i,j+1,k}, \Omega_{i,j,k+1}\},$$
$$S_8 = \{\Omega_{ijk}, \Omega_{i-1,j,k}, \Omega_{i,j+1,k}, \Omega_{i,j,k-1}\}.$$

The performances are comparable for the two types of candidate sub-stencils. For simplicity, the index of elements of the sub-stencils is also rearranged as follows

$$S_m = \{\Omega_{i'}^m, i' = 0, \ldots, 4\},$$

where $m = 1, \ldots, 8$. The following constrains need to be satisfied in the big stencil

$$\frac{1}{|\Omega_{i'}|} \int \int \int_{\Omega_{i'}^m} P_m(\boldsymbol{x}) \mathrm{d}V = Q_{i'}^m, \ \ \Omega_{i'}^m \in S_m,$$

where $Q_{i'}^m$ is the call averaged variable with the rearranged index. An over determined linear system can be generated, and the coefficients $b_{\boldsymbol{n}}^m$ in Eq. (12) can be determined by the least square method.

With the reconstructed polynomial $P_m(\boldsymbol{x}), m = 0, \ldots, 8$, the point-value $Q(\boldsymbol{x}_G)$ and the spatial derivatives $\partial_x Q(\boldsymbol{x}_G), \partial_y Q(\boldsymbol{x}_G), \partial_z Q(\boldsymbol{x}_G)$ for reconstructed variables at Gaussian quadrature point can be given by the non-linear combination

$$Q(\boldsymbol{x}_G) = \overline{\omega}_0 \left(\frac{1}{\gamma_0} P_0(\boldsymbol{x}_G) - \sum_{m=1}^{8} \frac{\gamma_m}{\gamma_0} P_m(\boldsymbol{x}_G) \right) + \sum_{m=1}^{8} \overline{\omega}_m P_m(\boldsymbol{x}_G),$$

$$\partial_x Q(\boldsymbol{x}_G) = \overline{\omega}_0 \left(\frac{1}{\gamma_0} \partial_x P_0(\boldsymbol{x}_G) - \sum_{m=1}^{8} \frac{\gamma_m}{\gamma_0} \partial_x P_m(\boldsymbol{x}_G) \right) + \sum_{m=1}^{8} \overline{\omega}_m \partial_x P_m(\boldsymbol{x}_G),$$

$$\partial_y Q(\boldsymbol{x}_G) = \overline{\omega}_0 \left(\frac{1}{\gamma_0} \partial_y P_0(\boldsymbol{x}_G) - \sum_{m=1}^{8} \frac{\gamma_m}{\gamma_0} \partial_y P_m(\boldsymbol{x}_G) \right) + \sum_{m=1}^{8} \overline{\omega}_m \partial_y P_m(\boldsymbol{x}_G),$$

$$\partial_z Q(\boldsymbol{x}_G) = \overline{\omega}_0 \left(\frac{1}{\gamma_0} \partial_z P_0(\boldsymbol{x}_G) - \sum_{m=1}^{8} \frac{\gamma_m}{\gamma_0} \partial_z P_m(\boldsymbol{x}_G) \right) + \sum_{m=1}^{8} \overline{\omega}_m \partial_z P_m(\boldsymbol{x}_G). \tag{13}$$

where $\partial_x P_m(\boldsymbol{x}_G), \partial_y P_m(\boldsymbol{x}_G), \partial_z P_m(\boldsymbol{x}_G)$ can be obtained by taking derivatives of the candidate polynomials directly. The non-linear weights ω_m and normalized non-linear weights $\overline{\omega}_m$ are defined as

$$\overline{\omega}_m = \frac{\omega_m}{\sum_{m=0}^{M} \omega_m}, \ \ \omega_m = \gamma_m \left[1 + \left(\frac{\tau}{\beta_m + \epsilon} \right) \right],$$

where the linear weights $\gamma_0 = 0.9$ and $\gamma_i = 0.0125, i = 1, \ldots, 8$ in the computation, ϵ is a small positive number and the parameter τ is chosen as

$$\tau = \sum_{m=1}^{8} \left(\frac{|\beta_0 - \beta_m|}{8} \right)^2.$$

The smooth indicator β_m is defined as

$$\beta_m = \sum_{|l|=1}^{r_m} |\Omega_{ijk}|^{\frac{2|l|}{3}-1} \int_{\Omega_{ijk}} \left(\frac{\partial^l P_m}{\partial_x^{l_1} \partial_y^{l_2} \partial_z^{l_3}} (x, y, z) \right)^2 \mathrm{d}V, \tag{14}$$

where $r_0 = 2$ and $r_m = 1, m = 1, \ldots, 8$. Eq. (13) ensures a fourth-order accuracy and a brief proof is given. According to the Taylor expansion, the smooth indicator Eq. (14) can be rewritten as

$$\beta_0 = \left(\left(\frac{\partial Q}{\partial x} \right)^2 + \left(\frac{\partial Q}{\partial y} \right)^2 + \left(\frac{\partial Q}{\partial z} \right)^2 \right) \Big|_{\boldsymbol{x}_0} |\Omega_{ijk}|^{2/3} (1 + \mathcal{O}(|\Omega_{ijk}|^{2/3})),$$

$$\beta_m = \left(\left(\frac{\partial Q}{\partial x} \right)^2 + \left(\frac{\partial Q}{\partial y} \right)^2 + \left(\frac{\partial Q}{\partial z} \right)^2 \right) \Big|_{\boldsymbol{x}_0} |\Omega_{ijk}|^{2/3} (1 + \mathcal{O}(|\Omega_{ijk}|^{1/3})),$$

where $m = 1, \ldots, 8$. Therefore, the non-linear weights can be approximated as

$$\overline{\omega}_m \sim \omega_m = \gamma_m (1 + \mathcal{O}(h^2)),$$

For the quadratic polynomial $P_0(\boldsymbol{x})$, the error of approximation can be written as

$$P_0(\boldsymbol{x}_G) = q(\boldsymbol{x}_G) + A(\boldsymbol{x}_G) h^4 + \mathcal{O}(h^5),$$

where $Q(\boldsymbol{x}_G)$ is the exact solution at the Gaussian quadrature point $\boldsymbol{x}_G$. For the linear polynomial $P_m(\boldsymbol{x}_G)$, the error can be written as

$$P_m(\boldsymbol{x}_G) = q(\boldsymbol{x}_G) + B_m(\boldsymbol{x}_G) h^2 + \mathcal{O}(h^3),$$

The reconstructed point value with non-linear weights can be written as

$$Q(\boldsymbol{x}_G) = \frac{\overline{\omega}_0}{\gamma_0} P_0(\boldsymbol{x}_G) + \sum_{m=1}^{8} \left(\overline{\omega}_m - \frac{\overline{\omega}_0 \gamma_m}{\gamma_0} \right) P_m(\boldsymbol{x}_G),$$

$$= q(\boldsymbol{x}_G) + \frac{\overline{\omega}_0}{\gamma_0} (A(\boldsymbol{x}_G) h^3 + \mathcal{O}(h^4))$$

$$+ \sum_{m=1}^{8} \left(\overline{\omega}_m - \overline{\omega}_0 \frac{\gamma_m}{\gamma_0} \right) (B_m(\boldsymbol{x}_G) h^2 + \mathcal{O}(h^3))$$

$$= q(\boldsymbol{x}_G) + \left(A(\boldsymbol{x}_G) + \sum_{m=1}^{8} B_m(\boldsymbol{x}_G) \right) h^4 + \mathcal{O}(h^5).$$

Therefore, with the reconstructed point value and spatial derivatives, the spatial and temporal coupled gas-kinetic flow solver can be fully determined and the expected order of accuracy can be achieved.

Remark 1. As a feature of WENO type scheme, a very large stencil is needed which generates a large linear system, i.e. Eq. (11). In the code, the matrix $(\mathbf{A}^T \mathbf{W} \mathbf{A})^{-1} \cdot \mathbf{A}^T \mathbf{W}$ is restored for each cell, which requires a large memory. However, for the moving-mesh computation, the inverse procedure needs to be conducted every step and the efficiency will be reduced dramatically.

Thus, it is difficult to go further for the higher-order reconstruction in the current framework, and the development of high-order scheme with a compact stencil becomes demanding [22].

Remark 2. In order to eliminate the spurious oscillation and improve the stability, the reconstruction can be performed for the characteristic variables in the local coordinate. A simple limiting procedure is used to improve the robustness. For the reconstructed variables $P_m(\mathbf{x}_G)$, if any one value of the densities $\rho_m(\mathbf{x}_G)$ and pressures $p_m(\mathbf{x}_G)$ become negative, the derivatives are set as zero and first-order reconstruction is adopted.

4. Numerical tests

In this section, numerical tests for both inviscid and viscous flows will be presented to validate the current scheme. For the inviscid flows, the collision time τ takes

$$\tau = \epsilon \Delta t + C \left| \frac{p_l - p_r}{p_l + p_r} \right| \Delta t,$$

where $\epsilon = 0.01$ and $C = 1$. For the viscous flows, we have

$$\tau = \frac{\mu}{p} + C \left| \frac{p_l - p_r}{p_l + p_r} \right| \Delta t,$$

where p_l and p_r denote the pressure on the left and right sides of the cell interface, μ is the dynamic viscous coefficient and p is the pressure at the cell interface. In smooth flow regions, it will reduce to $\tau = \mu/p$. Without special statement, the specific heat ratio $\gamma = 1.4$ and CFL number $CFL = 0.35$ are used in the computation. In the numerical examples, the classical dimension-by-dimension fifth-order WENO-Z scheme [33] and the third-order WENO scheme [32] are usually tested as reference, which are abbreviated as WENO-5 and WENO-3 respectively. The current scheme is abbreviated as WENO-4.

4.1. Accuracy test

The advection of density perturbation for three-dimensional flows is presented to test the order of accuracy. For this case, the physical domain is $[0, 2] \times [0, 2] \times [0, 2]$ and the initial condition is set as follows

$$\rho_0(x, y, z) = 1 + 0.2 \sin(\pi(x + y + z)), \quad p_0(x, y, z) = 1,$$
$$U_0(x, y, z) = 1, \quad V_0(x, y, z) = 1, \quad W_0(x, y, z) = 1.$$

The periodic boundary conditions are applied at boundaries, and the exact solution is

$$\rho(x, y, z, t) = 1 + 0.2 \sin(\pi(x + y + z - t)), \quad p(x, y, z, t) = 1,$$
$$U(x, y, z, t) = 1, \quad V(x, y, z, t) = 1, \quad W(x, y, z, t) = 1.$$

The uniform meshes with $\Delta x = \Delta y = \Delta z = 2/N$ are tested. As reference, the L^1 and L^2 errors and order of accuracy at $t = 2$ for the WENO-3 reconstruction is given in Tab.1. For the WENO-4 reconstruction, the L^1 and L^2 errors and order of accuracy are presented in Tab.2, where the expected order of accuracy is achieved. The absolute errors as well as the convergence orders are improved by the WENO-4 reconstruction. The order of accuracy with non-coplanar meshes is also tested. For the non-coplanar meshes, the following mesh is considered

$$\begin{cases} x_i = \xi_i + 0.1 \sin(\pi \xi_i) \sin(\pi \eta_j) \sin(\pi \zeta_k), \\ y_j = \eta_j + 0.1 \sin(\pi \xi_i) \sin(\pi \eta_j) \sin(\pi \zeta_k), \\ z_k = \zeta_k + 0.1 \sin(\pi \xi_i) \sin(\pi \eta_j) \sin(\pi \zeta_k), \end{cases}$$

Table 1
Accuracy test: the advection of density perturbation for WENO-3 with uniform meshes.

Mesh	L^1 error	Order	L^2 error	Order
16^3	1.4612E−01		5.7820E−02	
32^3	2.0241E−02	2.8517	7.9355E−03	2.8651
64^3	2.5712E−03	2.9768	1.0083E−03	2.9763
128^3	3.2240E04	2.9955	1.2633E04	2.9966

Table 2
Accuracy test: the advection of density perturbation for WENO-4 with uniform meshes.

Mesh	L^1 error	Order	L^2 error	Order
16^3	5.8372E03		2.2805E03	
32^3	2.3680E04	4.6235	9.2951E05	4.6167
64^3	1.1556E05	4.3569	4.6539E06	4.3199
128^3	6.6095E07	4.1279	2.8008E07	4.0545

Table 3
Accuracy test: the advection of density perturbation for WENO-4 with non-coplanar meshes.

Mesh	L^1 error	Order	L^2 error	Order
16^3	1.0605E02		4.3992E03	
32^3	5.7093E04	4.2153	2.3355E04	4.2354
64^3	2.9764E05	4.2616	1.2228E05	4.2554
128^3	1.7431E06	4.0938	7.1849E07	4.0890

Table 4
Accuracy test: the advection of density perturbation for WENO-4 with moving meshes.

Mesh	L^1 error	Order	L^2 error	Order
16^3	1.4472E02		5.7134E03	
32^3	1.0741E03	3.7519	4.2541E04	3.7474
64^3	7.0181E05	3.9359	2.7789E05	3.9362
128^3	4.4374E06	3.9833	1.7564E06	3.9837

The L^1 and L^2 errors and orders of accuracy are presented in Tab.3, and the expected order of accuracy is achieved for the non-coplanar meshes as well. The fourth-order WENO scheme can be also implemented in the arbitrary-Lagrangian-Eulerian (ALE) formulation, and more details can be found in Pan et al. [34]. In this case, the time dependent mesh is given by

$$\begin{cases} x_i = \xi_i + 0.05 \sin(\pi \xi_i) \sin(\pi \eta_j) \sin(\pi \zeta_k) \sin \pi t, \\ y_j = \eta_j + 0.05 \sin(\pi \xi_i) \sin(\pi \eta_j) \sin(\pi \zeta_k) \sin \pi t, \\ z_k = \zeta_k + 0.05 \sin(\pi \xi_i) \sin(\pi \eta_j) \sin(\pi \zeta_k) \sin \pi t, \end{cases}$$

where $(\xi, \eta, \zeta) \in [0, 2] \times [0, 2] \times [0, 2]$ and (ξ_i, η_j, ζ_k) are given uniformly with $\Delta \xi = \Delta \eta = \Delta \zeta = 2/N$. The L^1 and L^2 errors and orders of accuracy at $t = 2$ are presented in Tab.4, and the expected order of accuracy is also achieved for moving-mesh computations.

4.2. Riemann problem

In this case, the one-dimensional and three-dimensional Sod problems are considered. The computational domain is $(x, y, z) \in [0, 1] \times [0, 1] \times [0, 1]$. For the one-dimensional problem, the initial conditions are given as follows

$$(\rho, U, V, W, p) = \begin{cases} (1, 0, 0, 0, 1), & 0 \le x < 0.5, \\ (0.125, 0, 0, 0, 0.1), & 0.5 < x \le 1, \end{cases}$$

where the non-reflection boundary conditions are imposed for all boundaries. For the three-dimensional problem, the initial conditions are given by

$$(\rho, U, V, W, p) = \begin{cases} (1, 0, 0, 0, 1), & 0 \le \sqrt{x^2 + y^2 + z^2} < 0.5, \\ (0.125, 0, 0, 0, 0.1), & 0.5 < \sqrt{x^2 + y^2 + z^2} \le 1, \end{cases}$$

where the symmetric boundary condition is imposed on the plane with $x = 0$, $y = 0$ and $z = 0$, and the non-reflection boundary condition is imposed on the plane with $x = 1$, $y = 1$ and $z = 1$. The exact solution of spherically symmetric problem can be given by the following one-dimensional system with geometric source terms

$$\frac{\partial Q}{\partial t} + \frac{\partial F(Q)}{\partial r} = S(Q),$$

where

$$Q = \begin{pmatrix} \rho \\ \rho U \\ \rho E \end{pmatrix}, F(Q) = \begin{pmatrix} \rho U \\ \rho U^2 + p \\ U(\rho E + p) \end{pmatrix}, S(Q) = -\frac{d-1}{r} \begin{pmatrix} \rho U \\ \rho U^2 \\ U(\rho E + p) \end{pmatrix}.$$

The radial direction is denoted by r, U is the radial velocity, d is the number of space dimensions. In the computation, the uniform mesh with $\Delta x = \Delta y = \Delta z = 1/100$ is used. The density, velocity and pressure profiles along $y = z = 0$ are given in Fig. 2 for 1D problem at $t = 0.2$ and for 3D problem at $t = 0.25$. The current scheme also well resolves the wave profiles and the symmetry of solution is well preserved.

4.3. Sedov problem

This is a three-dimensional explosion problem to model blast wave from an energy deposited singular point [24], which is used to test the robustness of spatial reconstruction especially for the Lagrangian and ALE computation. The initial density has a uniform unit distribution, and the pressure is 10^{-6} everywhere, except in the cell containing the origin. For this cell containing the origin, the pressure is defined as $p = (\gamma - 1)\varepsilon_0/V$, where $\varepsilon_0 = 0.106384$ is the total amount of released energy and V is the cell volume. The computational domain is $[0, 1.2] \times [0, 1.2] \times [0, 1.2]$, and the initial uniform meshes are used. In this case, the computation is performed in the ALE formulation and the grid velocity is given by the Lagrangian nodal flow solver [29]. Due to the singularity at the origin, a small CFL number $CFL = 0.01$ is used. After 10 steps, a normal CFL number is used. The symmetric boundary condition is imposed on the planes with $x = 0, y = 0, z = 0$, and the non-reflection boundary condition is imposed on the planes with $x = 1.2, y = 1.2, z = 1.2$. The solution consists of a diverging infinite strength shock wave whose front is located at radius $r = 1$ at $t = 1$ [24]. Initially, $20 \times 20 \times 20$ and $40 \times 40 \times 40$ uniform cells are used. The density profiles with respect to r at $t = 1$ are given in Fig. 3 and three-dimensional density distributions are given in Fig. 4. A sharp discontinuity is captured by the ALE computation, and the robustness of current scheme is validated by the case with strong discontinuity.

4.4. Taylor–Green vortex

This problem is aimed at testing the performance of high-order methods on the direct numerical simulation of a three-dimensional periodic and transitional flow defined by a simple initial condition, i.e. the Taylor–Green vortex [6,13]. With a uniform temperature field, the initial flow field is given by

$$u = V_0 \sin(\frac{x}{L}) \cos(\frac{y}{L}) \cos(\frac{z}{L}),$$

$$v = -V_0 \cos(\frac{x}{L}) \sin(\frac{y}{L}) \cos(\frac{z}{L}),$$

$$w = 0,$$

$$p = p_0 + \frac{\rho_0 V_0^2}{16}(\cos(\frac{2x}{L}) + \cos(\frac{2y}{L}))(\cos(\frac{2z}{L}) + 2).$$

The fluid is then a perfect gas with $\gamma = 1.4$ and the Prandtl number is $Pr = 0.71$.

Numerical simulations are conducted with two Reynolds numbers $Re = 280$ and 1600. The flow is computed within a periodic square box defined as $-\pi L \le x, y, z \le \pi L$. The characteristic convective time $t_c = L/V_0$. In the computation, $L = 1, V_0 = 1, \rho_0 = 1$, and the Mach number takes $M_0 = V_0/c_0 = 0.1$, where c_0 is the sound speed. The volume-averaged kinetic energy can be computed from the flow as it evolves in time, which is expressed as

$$E_k = \frac{1}{\rho_0 \Omega} \int_\Omega \frac{1}{2} \rho \boldsymbol{u} \cdot \boldsymbol{u} \mathrm{d}\Omega,$$

where Ω is the volume of the computational domain, and the dissipation rate of the kinetic energy is given by

$$\varepsilon_k = -\frac{\mathrm{d}E_k}{\mathrm{d}t}.$$

In the computation, the uniform mesh with $192 \times 192 \times 192$ mesh points is used. For the case with $Re = 280$, the normalized volume-averaged kinetic energy and dissipation rate are presented in Fig. 5, and the HGKS with WENO-3 reconstruction are presented as reference. The current results agree well with the reference data in Wang et al. [43], and WENO-3 scheme is much more dissipative. The case with $Re = 1600$ is also tested. The normalized volume-averaged kinetic energy and dissipation rate are presented in Fig. 5, and the current results agree well with the reference data [6]. As reference, the results of HGKS with WENO-5 scheme are presented, which performs better than the current scheme, especially at the peak of dissipative rate. The iso-surfaces of Q criterions colored by velocity magnitude for $Re = 280$ at $t = 5$ and 10 are shown in Fig. 7, and for $Re = 1600$ at $t = 10$ and 15 are shown in Fig. 8. For the case with $Re = 280$, the flow structure is relative simple. Meanwhile, the coherent structures breakdown at $t = 10$ for the case with $Re = 1600$. Beyond this breakdown, the flow is fully turbulent and the structures slowly decay until the flow comes to rest. For such complicated flows, more studies with HGKS can be found in Cao et al. [9] (Figs. 6 and 10).

4.5. Compressible isotropic turbulence

The compressible isotropic turbulence is regarded as one of cornerstones to elucidate the effects of compressibility for turbulence [26,37,44]. In this case, we concentrate on the decaying isotropic compressible turbulence without external force. The flow domain of numerical simulation is a cube box $0 \le x, y, z \le 2\pi$, with periodic boundary conditions in all three Cartesian directions for all flow variables. A three-dimensional solenoidal random initial velocity field is generated by a specified spectrum

$$E(\kappa) = A_0 \kappa^4 \exp(-2\kappa^2/\kappa_0^2), \tag{15}$$

where A_0 is a constant to get a specified initial kinetic energy, κ is the wave number, κ_0 is the wave number at which the spectrum peaks. The fixed A_0 and κ_0 in Eq. (15) are chosen for all cases, which are initialized by $A_0 = 0.00013$ and $\kappa_0 = 8$. Evolution of this artificial system is determined by initial thermodynamic quantities and two dimensionless parameters, i.e. the initial Taylor microscale Reynolds number and turbulent Mach number

$$Re_\lambda = \frac{(2\pi)^{1/4}}{4} \frac{\rho_0}{\mu_0} \sqrt{2A_0} \kappa_0^{3/2},$$

$$Ma_t = \frac{\sqrt{3}}{\sqrt{\gamma R T_0}} u_{rms},$$

where the initial density $\rho_0 = 1$ and u_{rms} is the root mean square of initial velocity field. With Re_λ, Ma_t and $\gamma = 1.4$, the initial viscosity μ_0, pressure p_0 and temperature T_0 can be determined. The dynamic velocity can be also given by
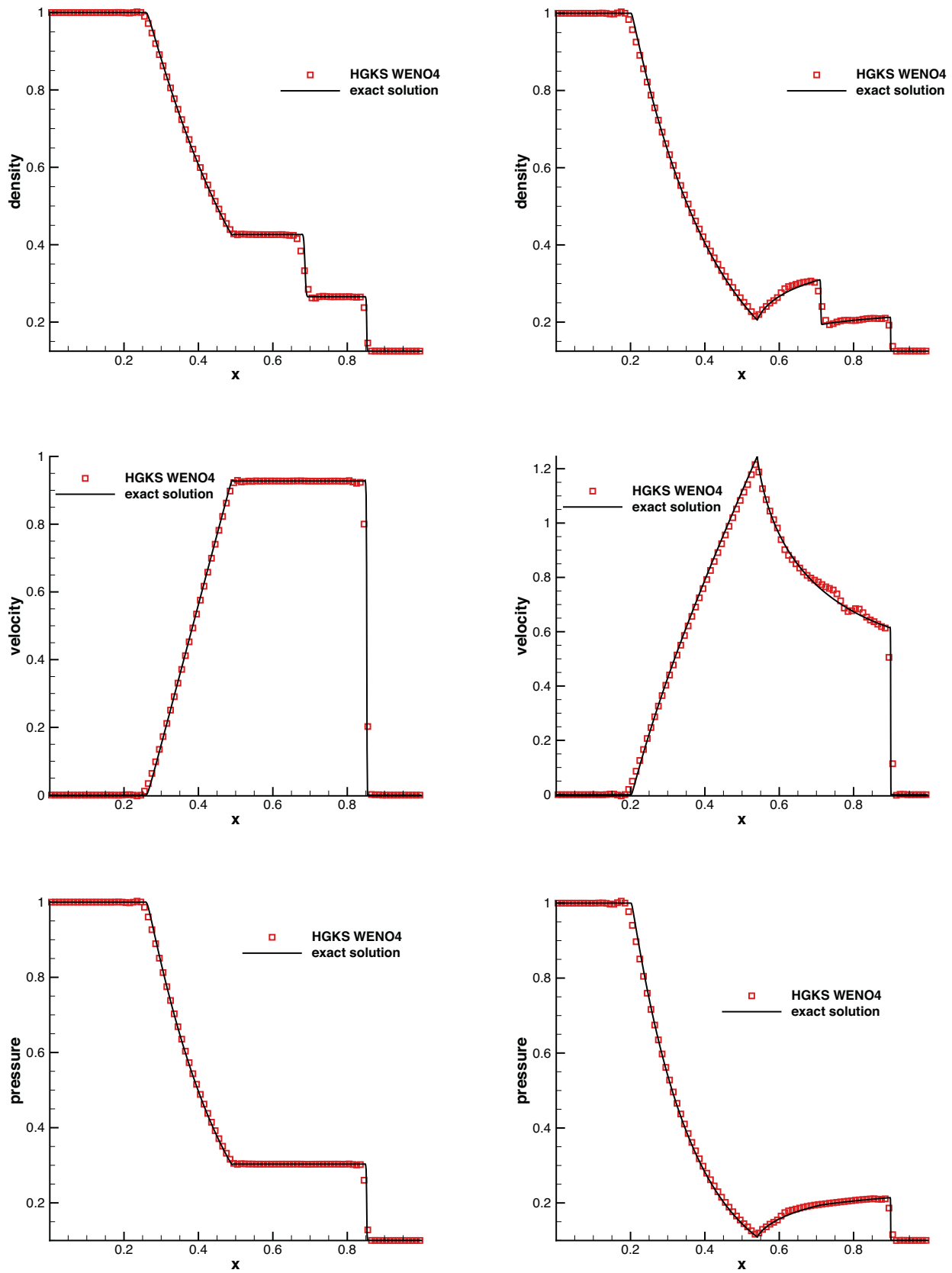
$$\mu = \mu_0(\frac{T}{T_0})^{0.76}.$$

Fig. 2. Sod problem: the density, velocity and pressure profiles along $y = z = 0$ for 1D problem at $t = 0.2$ (left) and 3D problem at $t = 0.25$ (right).
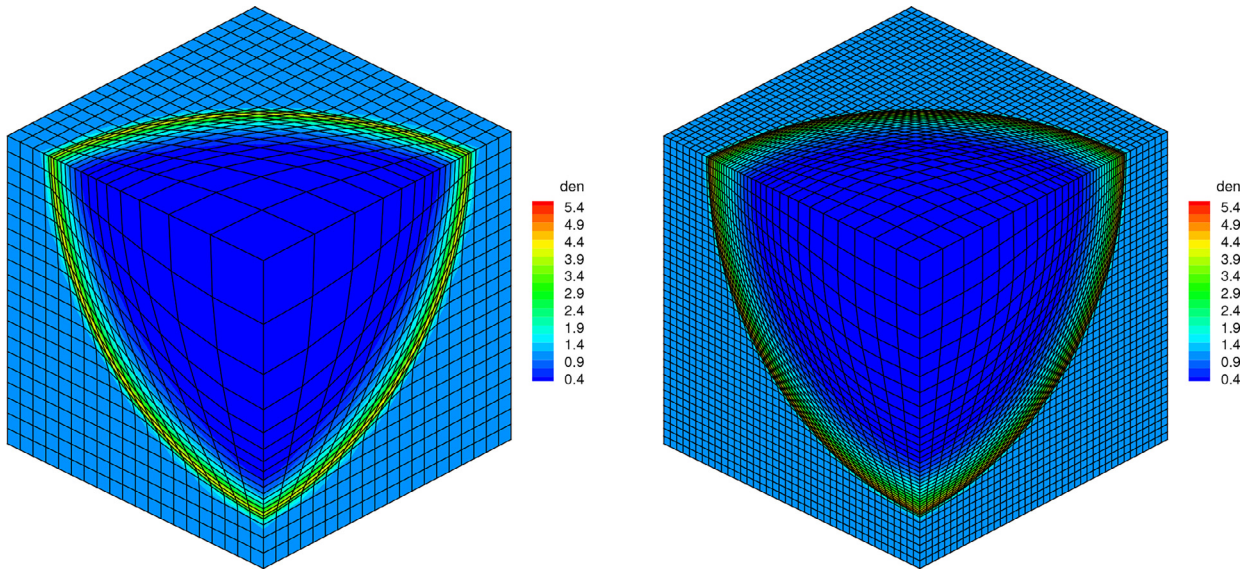
Fig. 3. Sedov problem: the three-dimensional density distributions at $t = 1$ for ALE computation with $20 \times 20 \times 20$ and $40 \times 40 \times 40$ cells.
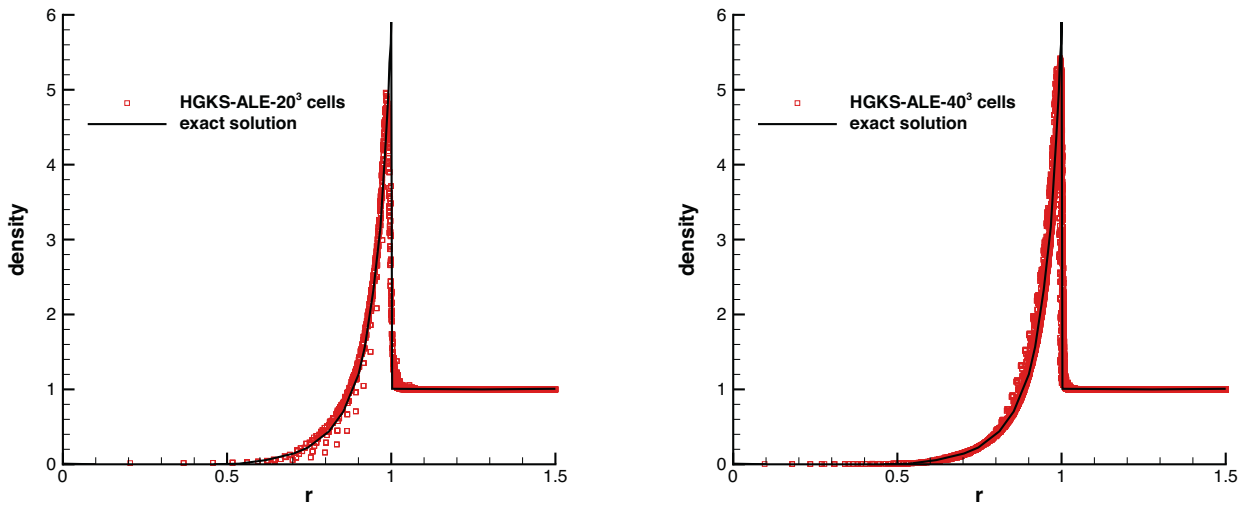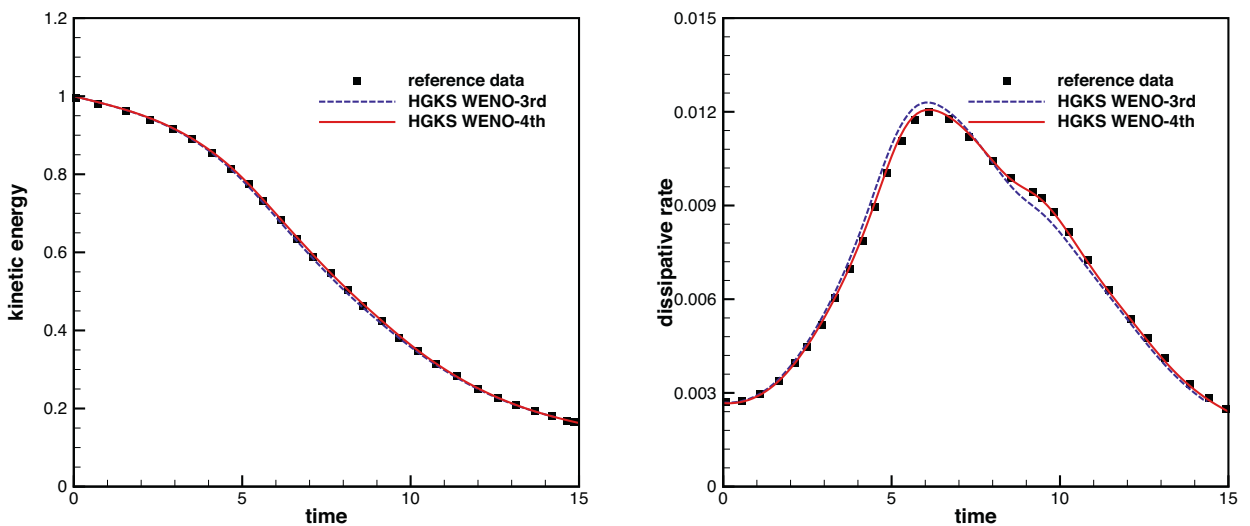

Fig. 4. Sedov problem: the density distributions with respect to r at $t = 1$ for ALE computation with $20 \times 20 \times 20$ and $40 \times 40 \times 40$ cells.

Fig. 5. Taylor–Greenvortex: the time history of kinetic energy E_k and dissipation rate $\varepsilon(E_k)$ for $Re = 280$.
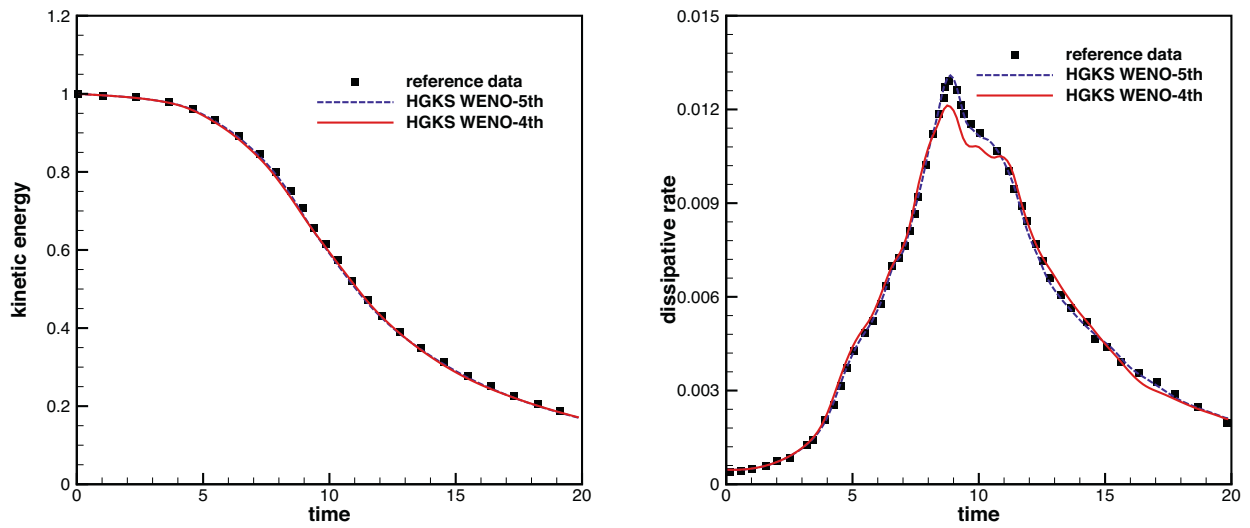
Fig. 6. Taylor–Greenvortex: the time history of kinetic energy E_k and dissipation rate $\varepsilon(E_k)$ for $Re = 1600$.
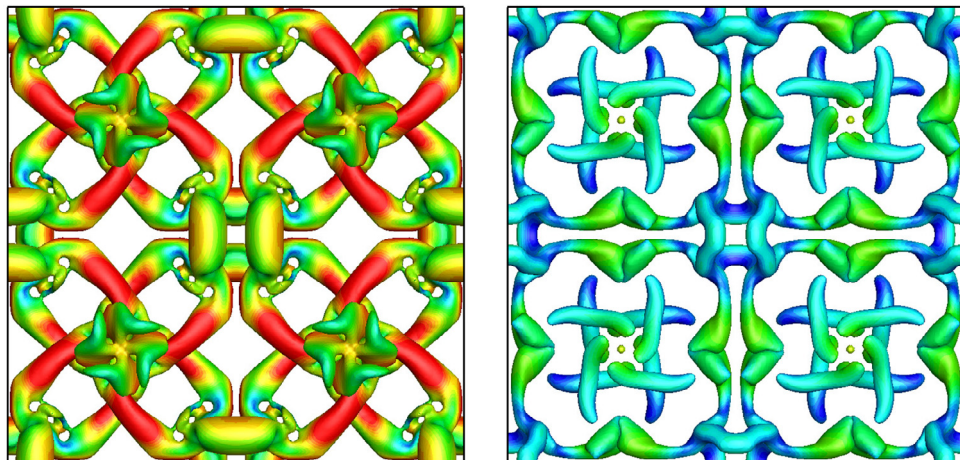
Fig. 7. Taylor–Greenvortex: the iso-surfaces of Q criterions colored by velocity magnitude at $t = 5$ and 10 for $Re = 280$.
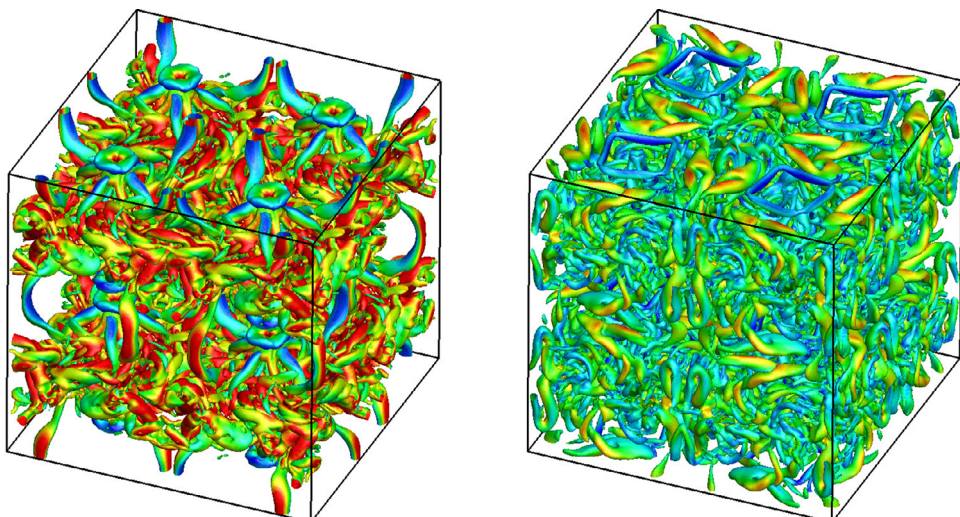
Fig. 8. Taylor–Greenvortex: the iso-surfaces of Q criterions colored by velocity magnitude at $t = 10$ and 15 for $Re = 1600$.
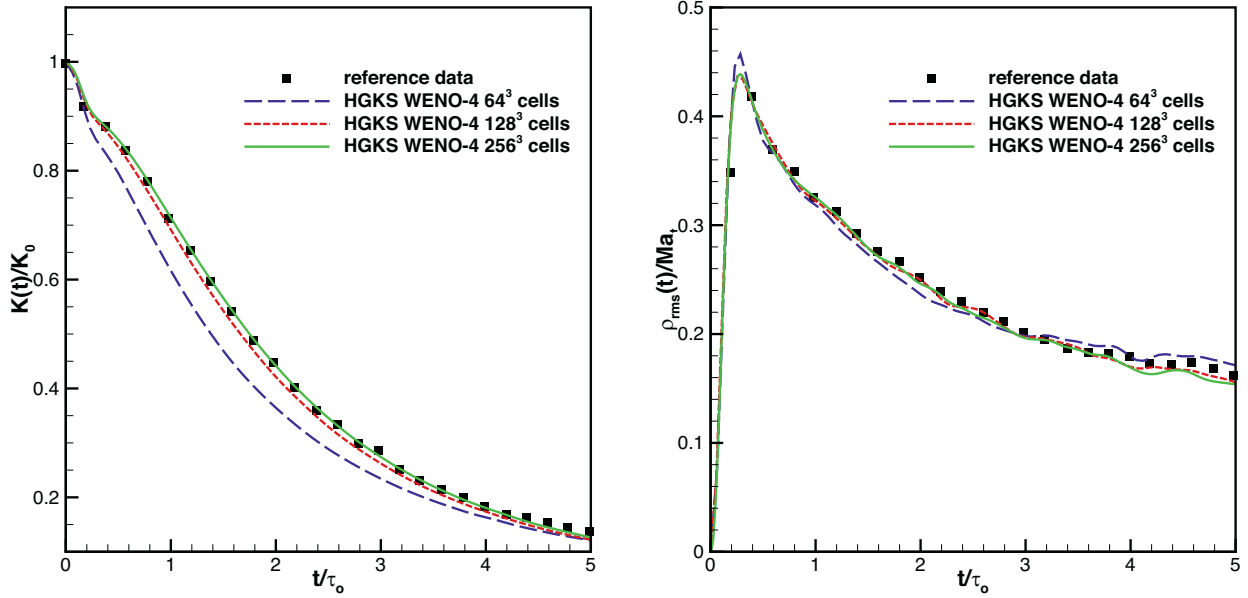
Fig. 9. Compressible isotropic turbulence: convergence study of the normalized turbulent kinetic energy and root-mean-square density fluctuation of WENO-4 reconstruction with $Ma_t = 0.5$.
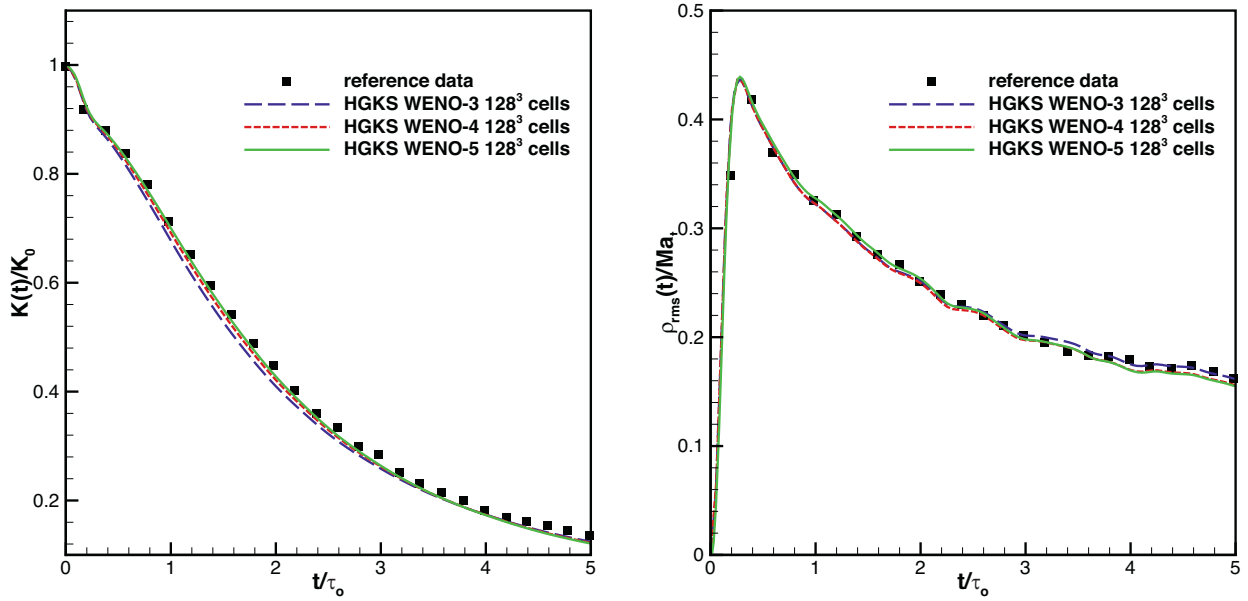
Fig. 10. Compressible isotropic turbulence: comparison of spatial reconstruction of the normalized turbulent kinetic energy and root-mean-square density fluctuation with $Ma_t = 0.5$.

With current initial strategy, the initial ensemble turbulent kinetic energy K_0, ensemble enstrophy Ω_0, ensemble dissipation rate ε_0, large-eddy-turnover time τ_{to}, Kolmogorov length scale η_0, and the Kolmogorov time scale τ_0 are given as

$$K_0 = \frac{3A_0}{64}\sqrt{2\pi}\kappa_0^5, \quad \Omega_0 = \frac{15A_0}{256}\sqrt{2\pi}\kappa_0^7, \quad \tau_{to} = \sqrt{\frac{32}{A_0}}(2\pi)^{1/4}\kappa_0^{-7/2},$$
$$\varepsilon_0 = 2\frac{\mu_0}{\rho_0}\Omega_0, \quad \eta_0 = (\nu_0^3/\varepsilon_0)^{1/4}, \quad \tau_0 = (\nu_0/\varepsilon_0)^{1/2}.$$

(16)

High-order compact finite difference method [44] was widely utilized in the simulation of compressible isotropic turbulence with moderate turbulent Mach number ($Ma_t \leq 0.8$). In the supersonic regime, the strong compression regions are close to several regions of high expansion, which pose much greater challenge for high-order schemes in supersonic regime. The compact finite difference scheme usually fails to capture strong shocklets. The flow

in subsonic regime with $Ma_t = 0.5$ is tested firstly. To test the convergence of current WENO-4 scheme, the time history of $\rho_{rms}(t)$ and $K(t)$ with 64^3, 128^3 and 256^3 uniform cells are given in Fig. 9, where the root-mean-square density fluctuation $\rho_{rms}(t)$ and the turbulent kinetic energy $K(t)$ are defined as

$$\rho_{rms}(t) = \sqrt{\langle(\rho - \langle\rho\rangle)^2\rangle},$$
$$K(t) = \frac{1}{2}\langle\rho\boldsymbol{U} \cdot \boldsymbol{U}\rangle.$$

The numerical results agree well with the reference data [37]. As expected, the current is less dissipative than WENO-3 scheme and more dissipative than WENO-5 scheme. To test the robustness of current scheme, the cases in the supersonic regime with $Ma_t = 0.8, 1.2, 1.6$ are also tested, where the mesh with 128^3 uniform cells is used. The time history of $\rho_{rms}(t)$ and $K(t)$ are presented in Fig. 11, and the numerical results agree well with the data pro-
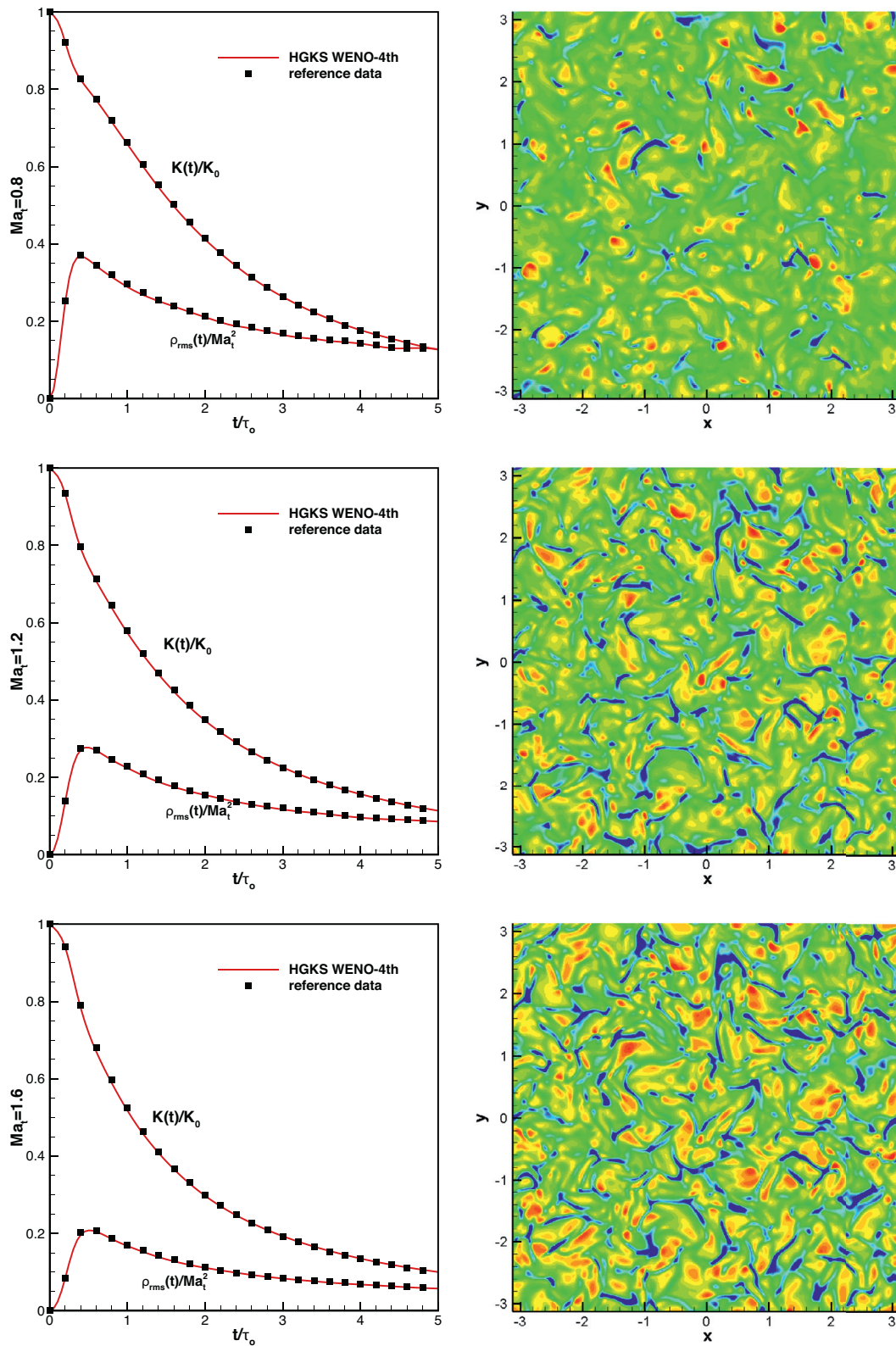
Fig. 11. Compressible isotropic turbulence: the normalized root-mean-square density, turbulent kinetic energy (left), and the contours of dilation $\theta = \nabla \cdot \boldsymbol{u}$ at $t/\tau_o = 1$ (right) with $Ma_t = 0.8$, 1.2 and 1.6.
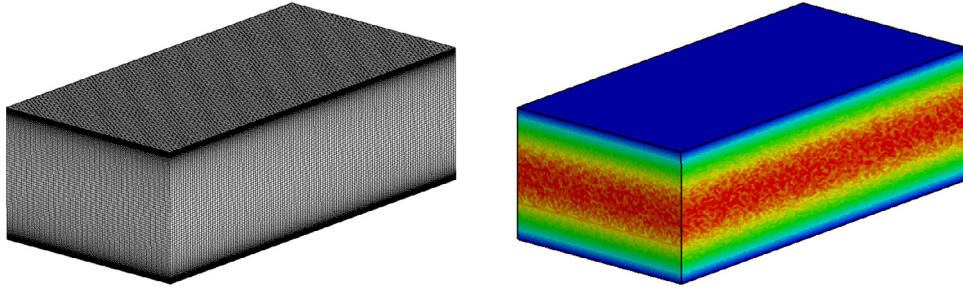
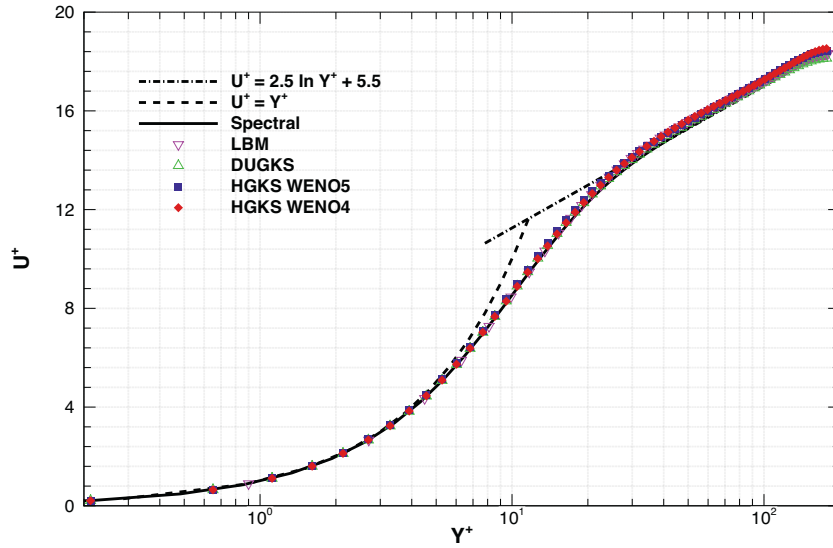**Fig. 12.** Turbulent channel flow: the mesh and initial streamwise velocity distributions.

Fig. 13. Turbulent channel flow: the mean flow velocity in log-linear plots for $Re_\tau = 180$.

vided by WENO-5 scheme. The contours of dilation $\theta = \nabla \cdot \boldsymbol{u}$ at $t/\tau = 1$, where the compression regions behave in the shape of narrower and longer "ribbon" with the increase of Ma_t.

4.6. Turbulent channel flow

Considering the simplicity of geometry and boundary conditions, the turbulent channel flows have been studied to understand the mechanism of wall-bounded turbulent flows. A large number of computational studies of turbulent channel flows have been carried out [25,30,31].

In the current study, the turbulent channel flow with friction Reynolds number $Re_\tau = 180$ is tested. The physical domain is $(x, y, z) \in [0, 2\pi] \times [-1, 1] \times [0, \pi]$ and the computational domain takes $(\xi, \eta, \zeta) \in [0, 2\pi] \times [0, 3\pi] \times [0, \pi]$. The coordinate transformation is given by

$$\begin{cases} x = \xi, \\ y = \tanh(b_g(\frac{\eta}{1.5\pi} - 1))/\tanh(b_g), \\ z = \zeta, \end{cases}$$

where $b_g = 2$. The periodic boundary conditions are used in streamwise x-direction and spanwise z-directions, and the non-slip and isothermal boundary conditions are used in vertical y-direction. Then, the external force based on the constant moment flux is used. The fluid is initiated with $\rho = 1$, $Ma = 0.1$ and the initial streamwise velocity profile is given by the perturbed Poiseuille flow profile

$$U(y) = 1.5(1 - y^2) + \text{white noise}.$$

White noise is added with 10% of local streamwise velocity. The friction Reynolds number is defined as

$$Re_\tau = \rho u_\tau H/\mu,$$

where $H = 1$ is the half height of the channel and the frictional velocity u_τ is given by

$$u_\tau = \sqrt{\frac{\tau_{wall}}{\rho}}, \quad \tau_{wall} = \mu \frac{\partial U}{\partial y}|_{wall}.$$

The plus unit and plus velocity are defined as

$$Y^+ = \rho u_\tau y/\mu, \quad U^+ = u/u_\tau.$$

The frictional velocity is determined by $u_\tau = U_c/U_c^+$, where $U_c = 1$ is the averaged velocity and U_c^+ is given by the logarithmic formulation for the channel flow.

$$U^+ = \frac{1}{\kappa} \ln Y^+ + B, \tag{17}$$

where von Karman constant $\kappa = 0.4$, $B = 5.5$ [25].

This case is tested with the direct numerical simulation firstly. For this case, the mesh with $128 \times 128 \times 128$ cells is used, where the grid points distributes uniformly in computational domian. Due to the explicit computation of high-order gas-kinetic scheme, a simple parallel strategy is adopted, where the two-dimensional domain decomposition is used. In the computation, 256 cores are used, where the domain is divided into 16 parts in y-direction, 16 parts in z-direction and no division is used in x-direction, respectively. The data communication is handled by the message passing interface (MPI) libraries. The details of mesh are given in Table 5, where $\Delta y_{\min}^+$ and $\Delta y_{\max}^+$ are the minimum and maximum grid
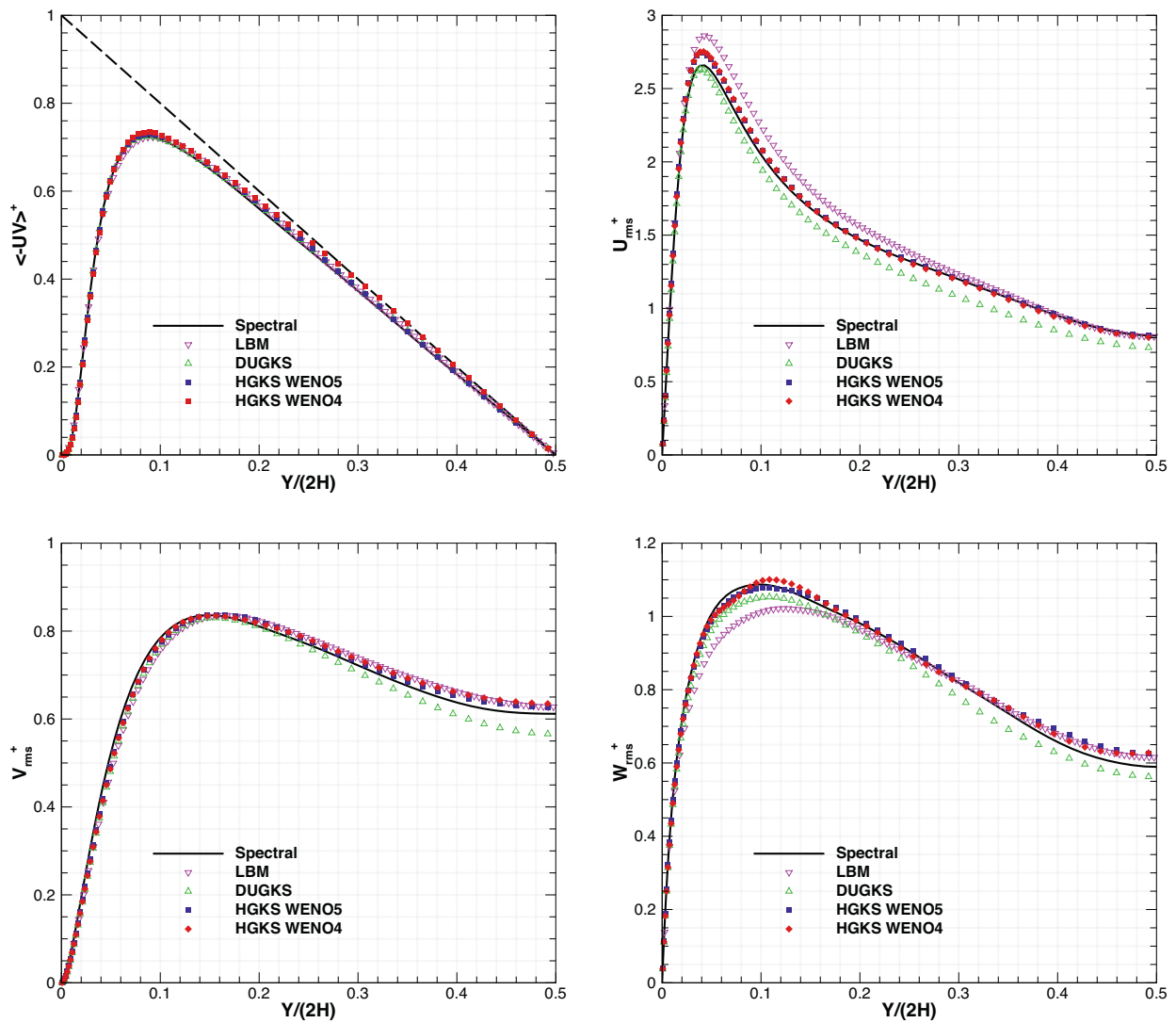
Fig. 14. Turbulent channel flow: the averaged Reynolds stress and root-mean-square velocity profiles for $Re_\tau = 180$.
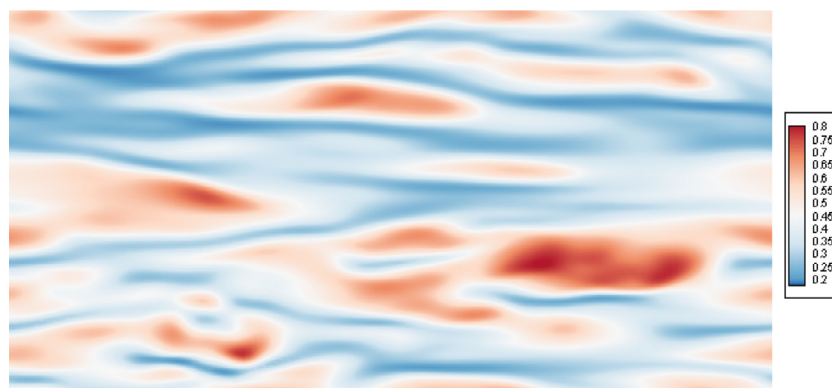

Fig. 15. Turbulent channel flow: distributions of streamwise velocity with $Y^+ = 8.5$.

space in the *y*-direction. As reference, the distribution of mesh and initial streamwise velocity in the physical domain are given in Fig. 12. The frictional velocity $u_\tau = U_c/U_c^+ = 0.0541$, where U_c^+ is given by Eq. (17) with $Y_c^+ = 180$ at the center line. This case is also tested by the HGKS using classical WENO-5 reconstruction [9] with the identical mesh. In a statistically stationary turbulent channel, the 200 periodic time as $200H/U_c$ is used. The mean

flow velocity is given in Fig. 13, and the averaged Reynolds stress and root-mean-square velocity profiles (turbulence intensities) are shown in Fig. 14. The current numerical results are in reasonable agreement with the spectral results, which is the first DNS result for the fully developed incompressible turbulent channel flow with $129 \times 192 \times 160$ grids [25]. The numerical results are also comparable with the results of WENO-5 based HGKS. As the most
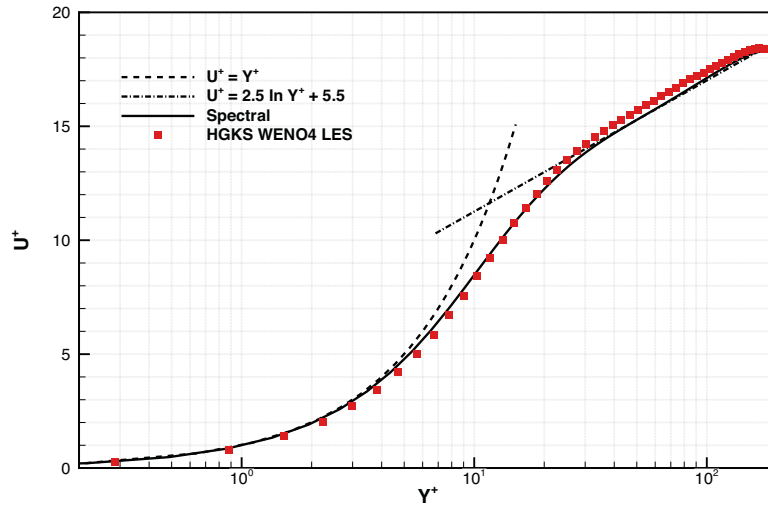
Fig. 16. Turbulent channel flow: the mean flow velocity in log-linear plots with $96 \times 96 \times 96$ cells for LES.
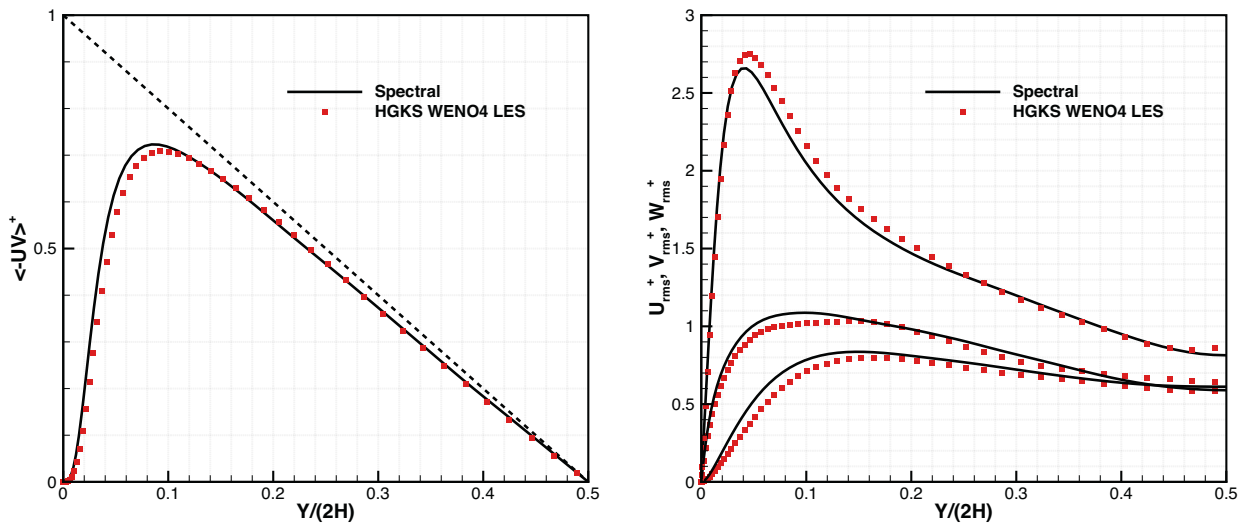

Fig. 17. Turbulent channel flow: the averaged Reynolds stress and root-mean-square velocity profiles for LES.

Table 5
Turbulent channel flow: different sets of grids.

Mesh size	$\Delta y^+_{min}/\Delta y^+_{max}$	Δx^+	Δz^+
96^3	0.29/7.76	11.77	5.89
128^3	0.21/5.83	8.83	4.42

popular mesoscopic methods for simulating nearly incompressible flows, the numerical results of the LBM with $200 \times 400 \times 200$ grids and DUGKS with $128 \times 128 \times 128$ grids are also presented [4]. Considering the good agreement in near-wall region and the near-center line region with the spectral benchmark, it is clear that HGKS outweighs LBM and DUGKS [4]. Fig. 15 shows the distributions of streamwise velocity with $Y^+ = 8.5$, and the near-wall streaks between the high-speed and low-speed fluids are observed, which is the dominant feature of the wall-turbulence.

This case is also tested with the large-eddy simulation with the Vreman-type LES model [42]. The numerical cell itself acts as the filter and no explicit filter is adopted in current scheme, and all the conserved macroscopic variables are calculated from gas-kinetic scheme. The turbulent viscosity μ_t is obtained from the LES eddy viscosity model, i.e. Eq. (5). In this case, no shock appears in the flow fields and an enlarged collision time is used in Eq. (8)

$$\tau_{total} = \tau + \tau_t = \frac{\mu + \mu_t}{p}.$$

In the computation, the mesh with $96 \times 96 \times 96$ cells is used, and the details of mesh is given in Table 5 as well. The mean flow velocity profile is presented in Fig. 16, and the resolved Reynolds stress and the r.m.s. fluctuation velocity are shown in Fig. 17. The profiles are generally in reasonable agreement with the DNS results, and the results slightly deviate from the DNS data in the buffer layer due to the insufficient grid resolution. A better agreement would be obtained if the resolved quantities were compared with the filtered DNS data, or compare unfiltered DNS data with the sum of the resolved and unresolved part from LES. Currently, no correction is implemented, and the reasonable deficiency of Reynolds stress and turbulence intensities from LES solutions are similar as the reference paper [42].

5. Conclusion

In this paper, a multi-dimensional fourth-order WENO reconstruction is presented, in which a simple strategy of selecting stencils for reconstruction is adopted and the topology independent linear weights are used. In corporate with two-stage fourth-order

temporal discretization, a fourth-order gas-kinetic scheme is developed for the direct numerical simulation and large eddy simulation of turbulent flows. The fourth-order reconstruction improves the order of accuracy of the previous third-order WENO reconstruction [32], which is too dissipative for the simulation of turbulent flows. Compared with the classical WENO reconstruction, the high-order accuracy can be also achieved for any non-uniform and curvilinear meshes in the finite volume framework. More importantly, the fourth-order reconstruction is robust and works well from the subsonic to hypersonic flows. Numerical results, from low speed to hypersonic flows, are provided to illustrate the good performance of such WENO reconstruction for turbulence simulation. The numerical results show the potential of current scheme in DNS and LES of turbulence. In the future, the current scheme will be extended to the genuinely three-dimensional unstructured mesh, and more challenging turbulent cases will be studied.

Declaration of Competing Interest

The authors declare that they have no known competing financial interests or personal relationships that could have appeared to influence the work reported in this paper.

CRediT authorship contribution statement

Liang Pan: Conceptualization, Writing - review & editing. **Guiyu Cao:** Conceptualization, Writing - review & editing. **Kun Xu:** Conceptualization, Writing - review & editing.

Acknowledgments

References

[1] Balsara DS, Garain S, Shu CW. An efficient class of WENO schemes with adaptive order. J Comput Phys 2016;326:780–804.

[2] Balsara DS, Garain S, Florinski V, Boscheri W. An efficient class of WENO schemes with adaptive order for unstructured meshes. J Comput Phys 2020;404:109062.

[3] Bhatnagar PL, Gross EP, Krook M. A model for collision processes in gases I: small amplitude processes in charged and neutral one-component systems. Phys Rev 1954;94:511–25.

[4] Bo YT, Wang P, Guo ZL, Wang LP. DUGKS simulations of three-dimensional Taylor–Greenvortex flow and turbulent channel flow. Comput Fluids 2017;155:9–21.

[5] Borges R, Carmona M, Costa B, Don WS. An improved weighted essentially non-oscillatory scheme for hyperbolic conservation laws. J Comput Phys 2008;227:3191–211.

[6] Bull J.R., Jameson A.. Simulation of the compressible Taylor–Green vortex using high-order flux reconstruction schemes. In: AIAA. 2014–3210.

[7] Cao GY, Su HM, Xu JX, Xu K. Implicit high-order gas kinetic scheme for turbulence simulation. Aerosp Sci Technol 2019;92:958–71.

[8] Cao GY, Pan L, Xu K. Three dimensional high-order gas-kinetic scheme for supersonic isotropic turbulence I: criterion for direct numerical simulation. Comput Fluids 2019;192:104273.

[9] Cao G.Y., Pan L., Xu K.. High-order gas-kinetic scheme with parallel computation for direct numerical simulation of turbulent flows. arXiv:2005.08736v1

[10] Chapman S, Cowling TG. The mathematical theory of non-uniform gases. 3rd ed. Cambridge University Press; 1990.

[11] Cockburn B, Shu CW. TVB Runge–Kutta local projection discontinuous Galerkin finite element method for conservation laws II: general framework. Math Comput 1989;52:411–35.

[12] Cockburn B, Shu CW. The Runge–Kutta discontinuous Galerkin method for conservation laws V: multidimensional systems. J Comput Phys 1998;141:199–224.

[13] Debonis J. Solutions of the Taylor–Green vortex problem using high-resolution explicit finite difference methods. AIAA paper; 2013. 2013-0382

[14] Du ZF, Li JQ. A hermite WENO reconstruction for fourth order temporal accurate schemes based on the GRP solver for hyperbolic conservation laws. J Comput Phys 2018;355:385–96.

[15] Dumbser M, Kaser M. Arbitrary high order non-oscillatory finite volume schemes on unstructured meshes for linear hyperbolic systems. J Comput Phys 2007;221:693–723.

[16] Germano M, Piomelli U, Moin P, Cabot WH. A dynamic subgrid-scale eddy viscosity model. Phys Fluids A 1991;3:1760–5.

[17] Harten A. A high resolution scheme for the computation of weak solutions of hyperbolic conservation laws. J Comput Phys 1983;49:357–93.

[18] Harten A, Engquist B, Osher S, Chakravarthy SR. Uniformly high order accurate essentially non-oscillatory schemes, III. J Comput Phys 1987;71:231–303.

[19] Henrick A, Aslam T, Powers J. Mapped weighted essentially non-oscillatory schemes: achieving optimal order near critical points. J Comput Phys 2005;207:542–67.

[20] Hu C, Shu CW. Weighted essentially non-oscillatory schemes on triangular meshes. J Comput Phys 1999;150:97–127.

[21] Ji X, Zhao FX, Shyy W, Xu K. A family of high-order gas-kinetic schemes and its comparison with Riemann solver based high-order methods. J Comput Phys 2018;356:150–73.

[22] Ji X, Zhao FX, Shyy W, Xu K. A HWENO reconstruction based high-order compact gas-kinetic scheme on unstructured mesh. J Comput Phys 2020;410:109367.

[23] Jiang GS, Shu CW. Efficient implementation of weighted ENO schemes. J Comput Phys 1996;126:202–28.

[24] Kamm JR, Timmes FX. On Efficient Generation of Numerically Robust Sedov Solutions; 2007.

[25] Kim J, Moin P, Moser R. Turbulence statistics in fully developed channel flow at low Reynolds number. J Fluid Mech 1987;177:133–66.

[26] Lele SK. Compact finite difference schemes with spectral-like resolution. J Comput Phys 1992;103:16–42.

[27] Li JQ, Du ZF. A two-stage fourth order time-accurate discretization for Lax–Wendroff type flow solvers I. Hyperbolic conservation laws. SIAM J Sci Comput 2016;38:3046–69.

[28] Liu XD, Osher S, Chan T. Weighted essentially non-oscillatory schemes. J Comput Phys 1994;115:200–12.

[29] Maire P-H, Abgrall R, Breil J, Ovadia J. A cell-centered lagrangian scheme for two-dimensional compressible flow problems. SIAM J Sci Comput 2007;29:1781–824.

[30] Moin P, Mahesh K. Direct numerical simulation: a tool in turbulence research. Annu Rev Fluid Mech 1998;30:539–78.

[31] Moser R, Kim J, Mansour N. Direct numerical simulation of turbulent channel flow up to Re_τ = 590. Phys Fluids 1999;11:943.

[32] Pan L, Xu K. High-order gas-kinetic scheme with three-dimensional WENO reconstruction for the euler and Navier–Stokes solutions. Comput Fluids 2020;198:104401.

[33] Pan L, Xu K, Li QB, Li JQ. An efficient and accurate two-stage fourth-order gas-kinetic scheme for the Navier–Stokes equations. J Comput Phys 2016;326:197–221.

[34] Pan L, Zhao FX, Xu K. High-order ALE gas-kinetic scheme with unstructured WENO reconstruction. J Comput Phys 2020;417:109558.

[35] Pope SB. Turbulent flows. Cambridge University Press; 2000.

[36] Sagaut P. Large eddy simulation for incompressible flows: an introduction. Springer Science & Business Media; 2006.

[37] Samtaney R, Pullin DI, Kosovic B. Direct numerical simulation of decaying compressible turbulence and shocklet statistics. Phys Fluids 2001;13:1415–30.

[38] Spalart P, Allmaras S. A one-equation turbulence model for aerodynamic flows. 30th aerospace sciences meeting and exhibit; 1992.

[39] Shu CW, Osher S. Efficient implementation of essentially non-oscillatory shock-capturing schemes II. J Comput Phys 1989;83:32–78.

[40] Tan S, Li QB, Xiao ZX, Fu S. Gas kinetic scheme for turbulence simulation. Aerosp Sci Technol 2018;78:214–27.

[41] Toro EF. Riemann solvers and numerical methods for fluid dynamics. 3rd ed. Springer; 2009.

[42] Vreman AW. An eddy-viscosity subgrid-scale model for turbulent shear flow: algebraic theory and applications. Phys Fluids 2004;16(10):3670–81.

[43] Wang L, Anderson WK, Erwin T, Kapadia S. High-order discontinuous Galerkin method for computation of turbulent flows. AIAA J 2015;53:1157–71.

[44] Wang JC, Wang LP, Xiao ZL, Shi Y, Chen SY. A hybrid numerical simulation of isotropic compressible turbulence. J Comput Phys 2010;229:5257–79.

[45] Wilcox DC. Formulation of the $k-\omega$ turbulence model revisited. AIAA J 2008;46:2823–38.

[46] Xu K. Direct modeling for computational fluid dynamics: construction and application of unified gas kinetic schemes. World Scientific; 2015.

[47] Xu K. A gas-kinetic BGK scheme for the Navier–Stokesequations and its connection with artificial dissipation and Godunov method. J Comput Phys 2001;171:289–335.

[48] Zhao FX, Pan L, Wang SH. Weighted essentially non-oscillatory scheme on unstructured quadrilateral and triangular meshes for hyperbolic conservation laws. J Comput Phys 2018;374:605–24.

[49] Zhu J, Qiu JX. A new fifth order finite difference WENO scheme for solving hyperbolic conservation laws. J Comput Phys 2016;318:110–21.

[50] Zhu J, Qiu JX. New finite volume weighted essentially non-oscillatory scheme on triangular meshes. SIAM J Sci Comput 2018;40:903–28.

[51] Zhu J, Shu CW. A new type of third-order finite volume multi-resolution WENO schemes on tetrahedral meshes. J Comput Phys 2020;406:109212.